Characteristics of the Interannual and Decadal Variability in a General Circulation Model of the Tropical Atlantic Ocean

BOHUA HUANG AND J. SHUKLA

Center for Ocean–Land–Atmosphere Studies, Institute of Global Environment and Society, Inc., Calverton, Maryland

(Manuscript received 24 May 1996, in final form 6 February 1997)

ABSTRACT

A numerical simulation has been conducted using a general circulation model of the tropical Atlantic Ocean forced with observed monthly surface wind stress for 1964–87 and parameterized surface heat flux. The simulated sea surface temperature (SST) and upper-ocean heat content (HC) are used to examine the low-frequency variability in the ocean. A comparison with the SST observations shows that the model realistically simulates the major features of the decadal variability at the sea surface, such as the fluctuation of the SST dipole pattern (or the meridional gradient). It also produces interannual variations with timescales of two to three years.

The simulated HC anomalies are used to examine the variations of the thermocline depth and the effects of ocean dynamics. A principal oscillation pattern (POP) analysis is performed to distinguish the spatial structures of decadal and interannual variations. It is found that the interannual variations are associated with tropical oceanic waves, stimulated by the fluctuations of the equatorial easterlies, which propagate eastward along the equator and westward to the north and south, resulting in an essentially symmetric structure about the equator at these scales. The periods of these modes are determined by the meridional width of the equatorial wind anomaly. The decadal mode, however, is associated with the ocean's adjustment in response to a basinwide out-of-phase fluctuation between the northeast and southeast trade winds. For instance, forced by a weakening of the northeast winds and a simultaneous strengthening of the southeast winds, the thermocline deepens in a belt extending from 5°N in the west to the North African coast. At the same time, the thermocline shoals from the southeast coast to the equatorial ocean. The associated SST pattern exhibits a strong dipole structure with positive anomalies in the north and negative anomalies in the south. When the wind anomalies weaken, the warm water accumulated in the northern tropical ocean is released and redistributed within the basin. At this stage, the SST dipole disappears. In the framework of this separation of the variability into two dominant timescales, the extraordinarily large warm SST anomalies in the southeast ocean in the boreal summer of 1984 are a result of in-phase interference of the decadal and interannual modes.

1. Introduction

In the eastern tropical Atlantic Ocean, variability of the sea surface temperature (SST) is characterized by a strong annual expansion of cold water from the African coast to 30°W in boreal summer. This feature, however, is not unique: intense development of the equatorial ''cold tongue'' also occurs annually in the eastern tropical Pacific Ocean. The similarity of these two phenomena has lead to suggestions of a common mechanism (Mitchell and Wallace 1992; Xie 1994). In fact, similarities between these two oceans are not confined to their seasonality. It has been found that both the Atlantic and Pacific display active oscillations centered at the equator with periods of a few years (Zebiak 1993). In the tropical Pacific, this equatorial variability, known as the El Niño–Southern Oscillation, is the regionally dominant signal, associated with unstable air–sea interactions (Philander 1990). At longer periods, however, the similarities between the two oceans break down. The low-frequency signals in the Pacific are generally weaker than the ENSO cycle and are described as long-term modulations of ENSO (Wang 1995; Gu and Philander 1995). On the other hand, the tropical Atlantic Ocean is characterized by well-defined decadal variations, which are as strong as its interannual variability. Moreover, the spatial structure of the decadal fluctuations is different from that of the interannual fluctuations. The most significant SST decadal signals are found not in the equatorial but in the subtropical ocean (Servain et al. 1985; Servain 1991).

Both equatorial and subtropical SST anomalies in the tropical Atlantic show significant effects on the large-scale atmospheric circulation and climate over the adjoining regions. For instance, rainfall anomalies in northeast Brazil tend to be associated with SST anomalies of opposite signs to the north and south of the climatological location of the intertropical convergence zone, a pattern usually referred to as the ''SST dipole''

Corresponding author address: Dr. Bohua Huang, Center for Ocean-Land Atmosphere Studies, Institute of Global Environment and Society, Inc., 4041 Powder Mill Road, Suite 302, Calverton, MD 20705-3106.

(e.g., Hastenrath and Heller 1977; Moura and Shukla 1981; Nobre and Shukla 1996). Hemispheric asymmetry also appears in SST differences between extremely dry and wet years in sub-Saharan Africa (e.g., Lamb 1978a,b; Hastenrath 1984; Lough 1986; Lamb and Pepler 1991). On the other hand, there is evidence suggesting connections between equatorial SST and rainfall fluctuations on the Gulf of Guinea coast (Wagner and Da Silva 1994) and Angola (Hirst and Hastenrath 1983).

The mechanisms of these anomalous SST variations, however, have yet to be understood. In fact, present analyses of the SST measurements with different statistical methods have lead to contradictory characterizations of the dominant variability. Results from conventional empirical orthogonal function analyses of historical SST measurements roughly agree with the results of rainfall–SST correlation studies and derive the dipolelike anomaly as a major mode of the tropical Atlantic SST variability (e.g., see Servain 1991). On the other hand, Houghton and Tourre (1992) have questioned whether the ''dipole pattern'' really comes from coherent out-of-phase variability between the northern and southern oceans. Based on the results of a rotated EOF analysis, they argue that the SST variations in the north and south are unrelated.

The controversy raised in interpreting the SST measurements exhibits the complexity of the observed phenomena. Part of the complication seems to result from the multiplicity of timescales responsible for observed variations. As we have pointed out earlier, unlike the tropical Pacific, there is no single dominant frequency in the tropical Atlantic variability. Instead, it is characterized by at least two major time periods, one on an interannual scale (with periods of two to three years) and the other on a decadal scale (with a period around ten years) (see also, e.g., Servain 1991; Mehta and Delworth 1995). Since fluctuations with significantly different timescales could be caused by different underlying mechanisms, it is useful to examine their features separately. However, the statistical tools used in previous studies, such as compositing based on certain climatic indices, various EOF techniques, and correlation analyses, may not be the most appropriate way in this respect.

Moreover, in order to understand the mechanisms of SST change, it is necessary to analyze the effects of surface heat flux, mixed layer physics, and the ocean circulation. At present, observations are not adequate to carry out such extensive diagnostic studies. However, simulations from state-of-the-art ocean general circulation models (OGCM) may be useful in compensating the sparseness of the oceanographic observations and provide a more comprehensive picture. It has been demonstrated that, when forced with climatological surface wind stress and parameterized surface heat fluxes, present OGCMs can produce a realistic mean state and annual cycle of the upper-ocean thermal structure and currents in the tropical Atlantic Ocean (e.g., see Philander and Pacanowski 1986; Richardson and Philander 1987; Schott and Böning 1991; Didden and Schott 1992; Huang 1992). There have been extensive verifications of model simulations forced by real-time winds against oceanographic observations collected in the Seasonal Equatorial Atlantic Ocean/Français Océan Climat dans l'Atlantique Equatorial (SEQUAL/FOCAL) experiments during 1982–84 (e.g., Reverdin et al. 1991; Blanke and Delecluse 1993). In general, these studies show that the observed interannual fluctuations of the thermocline depth during those years, especially the considerable thermocline deepening characteristic of the 1984 warm event in the Gulf of Guinea, can be captured reasonably well by these ocean models.

In recent years, several studies on the modeling and simulation of the interannual variability in the tropical Atlantic have been conducted at the Center for Ocean–Land–Atmosphere Studies (Huang 1992; Carton and Huang 1994; Huang et al. 1995; Huang and Shukla 1996). The chosen period (1980–88) for these studies is characterized by exceptionally active interannual changes in the ocean, with two strong warm events (1984 and 1987–88) in the Gulf of Guinea and a major transition of phase in the SST dipole pattern (or the anomalous meridional SST gradient) during 1984–85. The results of these studies show that the basinwide SST fluctuations in the 1980s, such as the fluctuation of the SST dipole and the occurrence of the equatorial warm events in 1984 and 1987–88, can be simulated realistically by an OGCM forced with observed wind stress and parameterized heat flux. In particular, Huang et al. (1995) demonstrated that there are significant variations of the oceanic circulation and thermal structure associated with both the dipole and equatorial SST fluctuations in this period. An out-of-phase fluctuation of the northeast and southeast trade wind systems was able to generate not only the equatorial propagation but also the basinwide redistribution of the upper-ocean heat content. However, these nine-year simulations are not long enough for us to distinguish the relatively higher frequency interannual variations and the lower frequency decadal signals.

In the present work, we have examined a longer period simulation for 1964–87, forced with observed surface winds. The model fields of 24-yr length permit a clearer separation between the decadal and interannual timescales so that their structures and development can be investigated. In the subsequent sections, we describe this simulation and examine the characteristics of its interannual and decadal variability. In analyzing this simulation, we concentrate on the fluctuations of both the upper-ocean heat content and SST, as well as their associations with the change of the surface wind stress and heat flux. In order to distinguish the interannual and decadal variations of the upper ocean, we use the technique of principal oscillation pattern (POP) analysis, which extracts space and time modes from complicated datasets based on timescale.

Our results show that variations on these two timescales have distinctly different spatial structures that can be traced back to their responses to different forcings. The interannual fluctuations are composed of tropical waves largely forced by equatorial wind fluctuations. The decadal fluctuations, however, are associated with the basinwide redistribution of the upper-ocean heat content in response to out-of-phase fluctuations of the northeast and southeast trade wind systems. The decadal SST fluctuations are caused by both the surface momentum and heat fluxes associated with this pattern of wind fluctuations.

2. Experimental design

The ocean general circulation model used for this study is a finite-difference treatment of the primitive equations of motion using the Boussinesq and hydrostatic approximations in spherical coordinates (Pacanowski et al. 1993). Its domain is that of the Atlantic Ocean between 30°S and 50°N. The coast line and bottom topography are realistic except that ocean depths less than 100 m are set to 100 m and the maximum depth is set to 4000 m. The zonal resolution was chosen to be 1.5°. The meridional grid spacing is 0.5° between 10°S and 10°N, gradually increasing to 1.5° at 20°S and 20°N. There are 20 levels in the vertical with a constant level interval of 15 m for the top 10 levels. The intervals of the lower 10 levels are 15.2, 16.1, 20.0, 34.1, 75.9, 177.1, 375.9, 687.4, 1063.8, and 1384.5 m. Richardson-number-dependent coefficients are chosen for the vertical mixing and diffusion of momentum, heat, and salinity (Pacanowski and Philander 1981). The horizontal viscosity and diffusivity are prescribed as constant with values 2×10^7 cm^2 s^{-1}.

The ocean is forced by the prescribed surface wind stress and the heat flux. The wind stress dataset is obtained from monthly pseudostress constructed by Servain and collaborators (Servain et al. 1987) from historical ship observations for 1964–87, which have been examined in previous studies (e.g., Servain et al. 1985; Servain and Legler 1986). The monthly pseudostress was originally derived by averaging observations in 5° × 2° boxes from 60°W to the African coast within 20°S–30°N. An objective analysis was then done to obtain fields on a 2° × 2° grid (Servain et al. 1987). We calculated the monthly surface wind stress from pseudostress by multiplying by the air density ρ and drag coefficient C_D. Since no suitable observations are available, ρ was fixed as 1.2×10^{-3} g cm^{-3}; C_D is derived based on the formulation of Trenberth et al. (1990), using the Comprehensive Ocean Atmosphere Data Set (COADS) monthly climatology to calculate the effect of stability. In those regions of the model domain for which this stress dataset is not available, the monthly climatological wind stress based on the European Centre for Medium-Range Weather Forecasts (ECMWF) twice-daily analyses for 1980–88 was used. The merging of the two datasets is done after both are linearly interpolated onto appropriate ocean model grids. A smoothing procedure is applied at the boundaries between the two datasets.

The surface heat flux is composed of solar radiative, longwave radiative, sensible, and evaporative components. The solar radiation is prescribed directly at the sea surface as the climatological monthly mean analyzed by Oberhuber (1988) for each month from the COADS data. Apart from using solar radiative flux as a boundary forcing, the design of this model permits heating within the upper ocean due to the penetration of solar radiation with an e-folding depth of 12 m. The longwave radiative fluxes are parameterized based on an empirical formula using the prescribed surface air temperature and model SST, following Rosati and Miyakoda (1988). The latent and sensible heat fluxes are parameterized based on bulk aerodynamic formulae dependent upon specified surface wind speed, air temperature, and the model-produced SST. The formulation and parameters used for these two components are the same as Philander and Pacanowski (1986). In these parameterizations, the surface air temperature is prescribed to be monthly climatological value from multiyear observations (Oort 1983). The surface wind speed is obtained from the observed monthly wind stress, which changes both annually and interannually.

Based on the parameterization, the model mean SST annual cycle tends to follow the prescribed monthly climatological surface air temperature. This may be problematic because, although the surface air temperature is close to the SST in reality, it is the air temperature that adjusts to the SST and not the other way around in the open ocean (for more discussions, see, e.g., Seager et al. 1988). As a result, part of the correct solution has been built into the mean annual cycle of the model SST fields. For this study, the problem is not that serious. Since we prescribed the climatological rather than the observed monthly surface air temperature in calculating the heat flux, the model SST anomalies can only be generated by wind fluctuations and ocean dynamics and are damped based on changes in the air–sea temperature difference. The damping, however, may be larger than they should be and might cause too weak SST anomalies, especially in the off-equatorial regions. Another problem of the parameterization is the neglect of the effects by cloudiness fluctuations on interannual periods.

The initial conditions for the experiment are an ocean at rest with January climatological temperatures and salinities (Levitus 1982). The model is spun up for six years forced with the monthly climatological wind stress, averaged from the period of 1964–87. Two model variables are used in the investigation: the SST and the upper-ocean heat content (HC). The latter is defined as the mean temperature of the upper 234 m, which approximately measures the fluctuations of thermocline depth, the sea level, or the dynamic height (Rebert

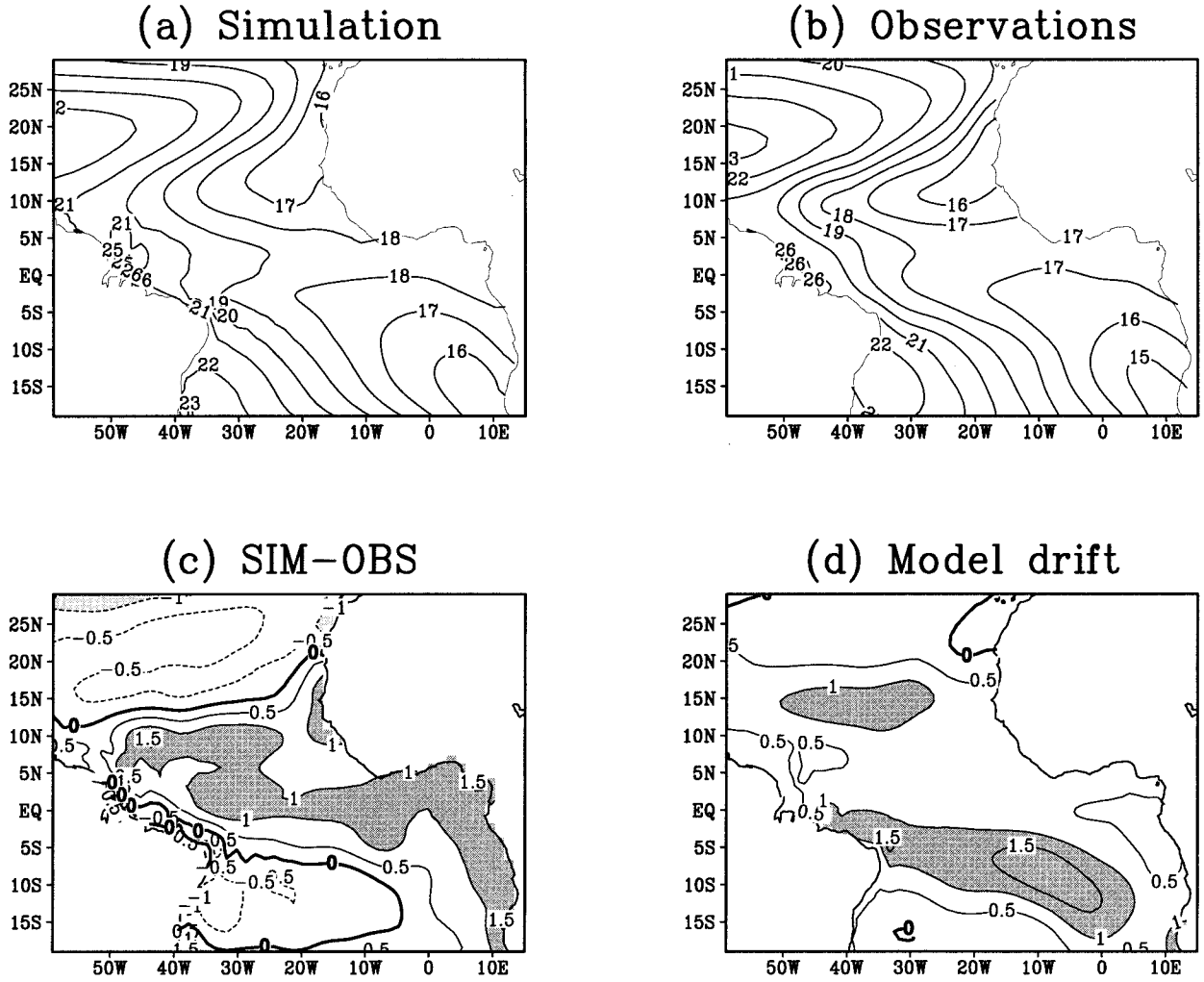

FIG. 1. Annual mean upper-ocean heat content (°C) in the tropical Atlantic Ocean from (a) simulation and (b) Levitus climatology. The difference between (a) and (b) is shown in (c). (d) The HC difference between averages in 1985–87 and in 1964–66. Contour interval is 1°C for (a) and (b) and 0.5 °C for (c) and (d). Regions with values greater than 1°C have dark shading and those with values less than −1°C have light shading in (c). Regions with values greater than 1°C are also shaded in (d).

et al. 1985). Our test shows that the HC variability is highly correlated to that of the depth of the 20°C isotherm in the tropical ocean. The simulated mean annual cycle is defined by a monthly climatology, taken to be the averages of the corresponding monthly mean values for the whole period of 1964–87. The signals of interannual and decadal variability are examined using the monthly anomalies from the climatological annual cycle.

3. The mean state

The mean state of the tropical Atlantic is shown here to provide the background for our discussion of the interannual and decadal variability. The discussion is based on the HC climatology because, as we have said before, the mean SST and its annual cycle are relaxed to observations and therefore do not reflect the effects of oceanic dynamics and wind forcing. The simulated annual mean HC for 1964–87 is shown in Fig. 1a. To compare the model result with observations, we have calculated the same quantity based on the monthly climatological temperatures from observations (Levitus 1982). The observed annual mean HC is shown in Fig. 1b. The main features of the HC are consistent between the simulation and observations (Figs. 1a,b).

The quantitative difference between the simulation and the observations is shown in Fig. 1c. The largest errors are in the equatorial ocean and along the eastern coast, where the mean temperature of the model is about 1°–1.5°C higher than the observations. In the subtropics of the northern and southern ocean, however, the model temperature is lower by 0.5°C. These systematic errors may partly be caused by errors in the forcing fields. The

warmer Tropics and colder extratropics in the model may also imply that the meridional heat transport is not adequate, which in turn could be linked to the model resolution.

The model climate also shows a slow drift caused by gradual diffusion in the lower thermocline. This artificial diffusion warms up the deeper ocean and cools down the upper ocean. The cooling, however, is mostly compensated by an increase in surface heat flux, which, depending on the prescribed air temperature and model SST, provides an unlimited heat source for the ocean. Therefore, when colder water upwells, it can always get heat at the sea surface. The whole tropical ocean gradually warms up due to this excessive heating. The warming proceeds slowly as a linear trend in the 30-yr integration. Figure 1d shows the difference between the HC averaged in the first three (1964–66) and last three (1985–87) years of this simulation. The spatial pattern of this difference is similar to the distribution for the rate of linear tendency derived from the HC fields. It shows that the climate drift is not uniform, which is largest near 5°N and 5°–10°S. Both represent weakening of the troughs in the vertically averaged temperature fields (Fig. 1a).

The tropical Atlantic Ocean is characterized by a strong annual cycle (e.g., see Katz 1987; Weigartner and Weisberg 1991). This annual cycle has been simulated successfully by OGCMs (e.g., Philander and Pacanowski 1986; Huang et al. 1995; Huang and Shukla 1996). The mean annual cycle produced by the present simulation is qualitatively similar to those reported in the previous studies.

4. Interannual and decadal variability

a. SST variability

Following Servain (1991), two indices of tropical Atlantic variability based on normalized SST anomalies are used to characterize the anomalous fluctuations in the tropical Atlantic Ocean: The dipole (DP) index is defined here as the difference between basin-averages in 4°–30°N and in 20°S–4°N and characterizes the SST dipole fluctuation (see Fig. 2a). The total basin (TB) index is the average within 20°S–30°N east of 60°W. These two indices were originally defined to quantify the temporal fluctuation of the two patterns of the observed SST anomalies based on conventional EOF analysis (Servain 1991). In fact, the DP index is used to characterize the dipole SST fluctuation that is usually derived as the second leading EOF mode in observations. The TB index is used to characterize the basinwide in-phase variations, derived as the first EOF mode in observations.

The indices calculated from the simulation and the observations are shown in Figs. 2b,c, where the observations for 1964–87 are based on the Servain et al. (1987) dataset derived in the same way as the winds. To eliminate high-frequency intraseasonal fluctuations, these indices are smoothed using a 3-month running mean. These results are very similar to Huang et al. (1995). For the DP index (Fig. 2b), the simulation (thin curve) reproduces a significant portion of the observed (thick curve) dipole fluctuations with a correlation coefficient of 0.62. This high correlation is achieved mainly through the consistency between the model and the observations at decadal scales, with mostly positive values (warm north/cold south) during 1978–82, and negative values (cold north/warm south) in 1972–76 and again after 1984.

The TB indices from the simulation and the observations (Fig. 2c) show coherent variations from the mid 1970s to the mid 1980s. In the earlier period, however, there is a considerable discrepancy. In comparison with the DP index, the TB index shows more fluctuations on interannual periods though there also seems to be a decadal modulation. For instance, the observed TB index tends to increase, beginning in the mid 1970s. On the other hand, the simulated TB index shows a strong decreasing trend during the first ten years, consistent with a similar trend of increasing winds averaged in the same domain. This trend in the wind stress fields is possibly an artifact of the changes in measurement techniques (Cardone et al. 1990).

Overall, the above comparison suggests that the model is able to reproduce the low-frequency fluctuation of the observed SST dipole pattern in this period quite realistically. Moreover, although the model cannot accurately simulate the timing of the basinwide interannual warm and cold episodes, some of their statistical features, such as the dominant timescales, are realistic. Since these relatively high-frequency episodes are mainly composed of warm and cold ''events'' in the eastern equatorial ocean in response to the fluctuations of the equatorial easterlies in the west (Servain et al. 1982), the error of the model in the timing may reflect errors in the wind observations, especially in the earlier periods.

Finally, the decadal fluctuations of the DP index do not necessarily mean the SST in the north and south has corresponding out-of-phase variations. In fact, correlations of SST anomalies averaged within the northern and southern parts of the ocean (areas denoted with ''N'' and ''S'' in Fig. 4a) are lower for both the simulation (0.25) and observations (0.17). Different explanations for this low correlation are given in Houghton and Tourre (1992) and Huang et al. (1995). The former suggest that the SST fluctuations are independent between the north and the south. The latter argue that even though the decadal signals are coherently out-of-phase between the two parts of the ocean, the effect of higher-frequency variability symmetric about the equator brings the correlation down. We carry out a more comprehensive analysis in the next section to address this important question.

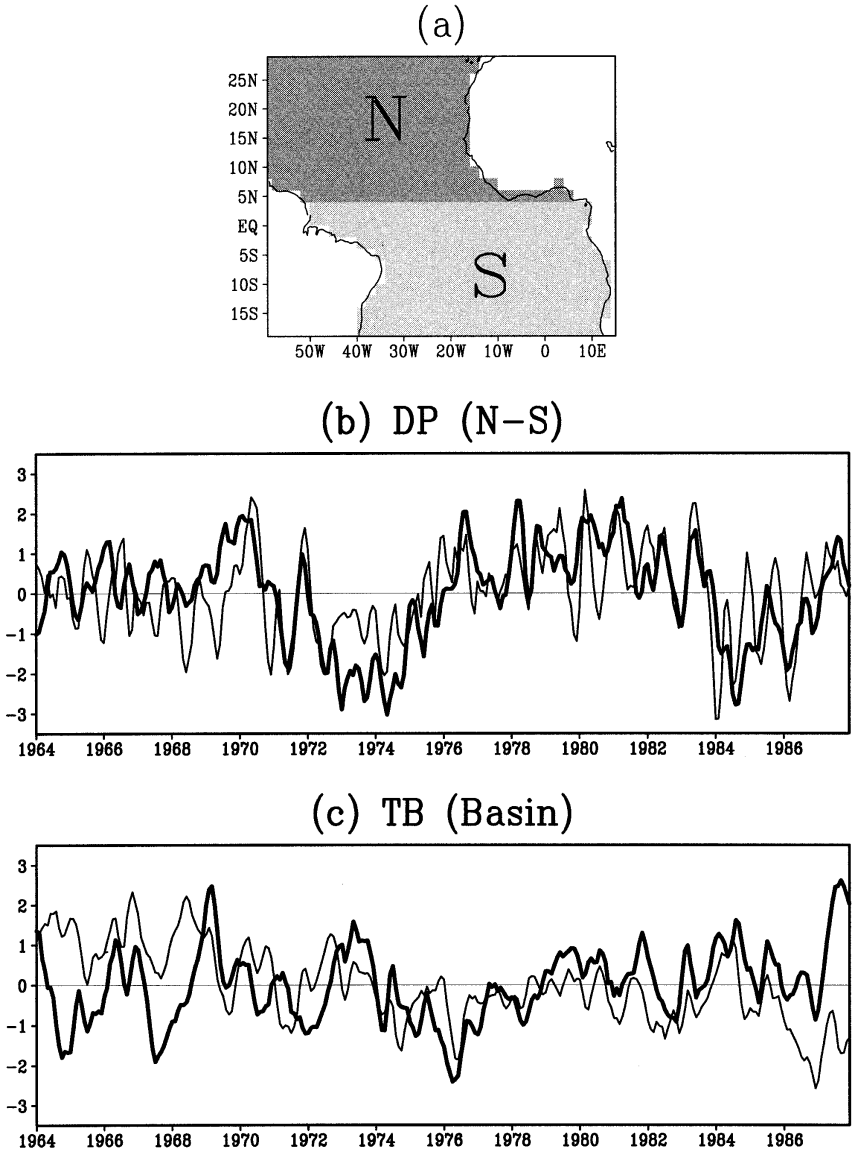

FIG. 2. (a) The areas averaged for defining the DP and TB indices of the SST anomalies in the tropical Atlantic Ocean. The DP and TB indices for 1964–87 are shown in (b) and (c) respectively. The thick line is for observations and the thin line for the simulation.

b. Principal oscillation pattern (POP) analysis of the HC field

We use the anomalous HC field to examine the oceanic processes on interannual and decadal timescales because it represents the fluctuations of the thermocline depth in response to the anomalously varying surface wind stress. To infer the space–time variations of this field, the principal oscillation pattern (POP) analysis is employed. The basic assumption of this technique is that the state vector $\mathbf{X}(t)$ of the field being analyzed satisfies the dynamics of a linear system so that the ''normal modes'' of the variations can be identified as the eigenvectors of this system. In particular, the eigenvectors associated with real eigenvalues represent the modes that simply decay temporally with certain timescales, but those associated with complex eigenvalues correspond to modes that oscillate between two spatial patterns with certain periods while decaying with time. The POP method has been widely used for analyzing complicated geophysical systems [see, von Storch et al. (1995) for a comprehensive review]. Its formulation is briefly described in the appendix.

There are advantages of using POP analysis to examine HC anomalies in preference to more traditional EOF analyses. First, the POP modes are calculated based on time periods so that the analysis is equivalent to a multivariate spectral analysis of vector time series (Hasselmann 1988). Moreover, the POP modes are not nec-

TABLE 1. Information on the POP modes derived from the simulated HC anomalies.

POP modes	Period (mo)	Damping time (mo)	Variance (%)
Real I (RI)	∞	60	23
Real II (RII)	∞	16	25
Complex I (CI)	117	28	28
Complex II (CII)	71	11	21
Complex III (CIII)	33	13	14
Complex IV (CIV)	18	6	19

essarily standing oscillations, as are those derived from EOFs, so that propagation in the domain can be detected. Both features are essential to our analysis.

Before performing the POP analysis, long-term trends in the data are eliminated by subtracting a linear trend from the HC anomaly at each grid point. As discussed in the last section, these trends are associated with model climate drift and account for a significant portion of the total HC variance. Besides showing a totally unrealistic tendency, they also violate the assumption of statistical stationarity for POP analysis. The trends are eliminated locally because the model drift is not uniform over the basin, as shown in Fig. 1d. However, it is possible that by this procedure some realistic signals with long periods ($>$ 20 yr) are also eliminated or distorted.

The state vector $\mathbf{X}(t)$ of the anomalous HC is derived in a reduced subspace because the original fields are highly correlated spatially and should have many fewer degrees of freedom than the number of model grids. For this purpose, the HC fields are reconstructed using the first ten modes of the conventional EOF analysis, which retains about 73% of the total variance. This treatment filters out small-scale temporal and spatial noise. Overall, the reconstructed fields are a very good approximation to the large-scale variability of the original data. The correlation coefficients between them are larger than 0.8 over most of the domain. The POP analysis is then carried out on the reduced dataset. The number of modes extracted from the analysis is dictated by the degrees of freedom of the system. In fact, four complex and two real POP modes are derived. Their major characteristics are summarized in Table 1. Based on their periods, two of the modes oscillate on decadal timescales (CI and CII) and the other two on interannual timescales (CIII and CIV). It should be pointed out that the decay times of the oscillating modes are all smaller than their periods so that these modes, even though oscillatory by nature, may not be self-sustained within the ocean. However, they represent the tendency of the ocean's response to different surface forcings. As will be shown below, the fundamental properties of the dominant variations are well captured by some of these POP modes.

To test the stability of the derived modes, we have repeated the POP analyses with HC anomalies reconstructed with 20 and 30 EOF modes, which account for

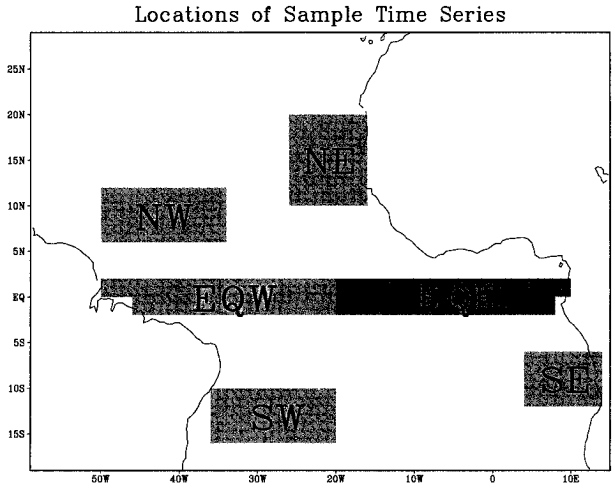

FIG. 3. The locations of sample time series. The shaded regions represent areas where average heat content is derived to represent oceanic variability in the northeast (NE), northwest (NW), western equatorial (EQW), eastern equatorial (EQE), southwest (SW), and southeast (SE) parts of the tropical Atlantic Ocean.

86% and 92% of the total variance respectively. As expected, more and more new modes appear with the increasing degrees of freedom. These new modes seem to come from two sources: one is localized small-scale features associated with information added by the higher EOF modes to the system. The other is the increased "spectral resolution" purely due to the increase in the degrees of freedom, which permit additional modes to form with frequencies between those derived in the lower-order subspace.

Despite these complications, all oscillating modes derived from our first analysis, except CII, seem to retain their major features in these higher subspaces. The corresponding modes in the lower- and higher-order subspaces is recognizable through their temporal and spatial structures as well as periods and decay times, although the latter two may be shifted by as much as several months. An examination has been done to see if any new information can be obtained from the analyses in subspaces with higher order. It seems that these new modes mainly add details to the processes identified from the lower-order analysis but do not reveal alternative physical processes. Therefore, we will mainly discuss the POP modes derived from the analysis of the reduced dataset using ten EOFs, but we note possible sensitivities by comparing with analyses from datasets using higher EOF modes and thus having more degrees of freedom.

Table 1 gives the ratio of the variance of each single POP mode to the total variance of the detrended but unfiltered HC anomalies (expressed as a percentage). Based on this table, it seems that most of the variance is contained in the pure decaying and lower-frequency oscillatory modes. However, it should be recognized that, unlike the EOF modes, the POP modes are not

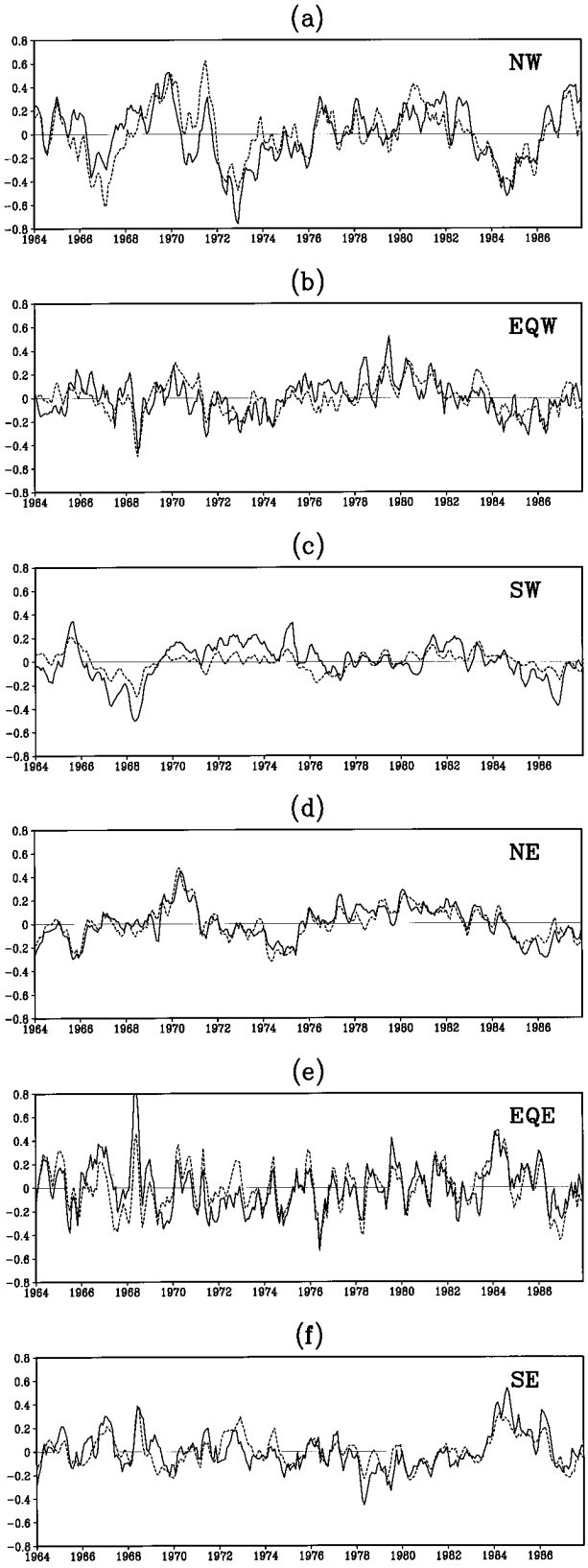

FIG. 4. Time series of the area-averaged HC anomalies at (a) NW, (b) EQW, (c) SW, (d) NE, (e) EQE, and (f) SE. For each panel, the solid curve is from the simulation and the dashed curve is from the reconstruction based on the three POP modes (CI, CIII, and CIV). Unit is degrees Celsius.

"orthogonal" so that time series of different modes can be significantly correlated. As a result, the total variance is not the sum of the variances of all the modes and therefore the percentage of variance explained is not necessarily the appropriate criterion to determine the importance of the modes. In fact, we found that the variance accounted for by the combination of the two real modes in Table 1 is just slightly higher than that by each of them due to their high negative correlation. Moreover, just considering the percentage of basin-accumulated total variance alone may undermine those modes that describe locally dominant processes. Actually, the interannual modes (CIII and CIV), though modest in explaining the total variance, are highly correlated with the original data in the equatorial and coastal regions where variations are most pronounced.

We have adopted an alternative procedure to select the important modes. We examined which modes as well as how many of them are needed to give a reasonable representation of all the anomalous HC time series averaged in the six areas shown in Fig. 3. These areas represent the northwest and northeast (NW and NE), western and eastern equatorial (EQW and EQE), as well as southwest and southeast (SW and SE) parts of the ocean. We recognize that this criterion is somewhat arbitrary because it is based on the choice of regions for examining the variability. However, previous studies have shown that the variabilities there seem to be good indicators of the major fluctuations in the basin (e.g., Servain et al. 1985; Huang et al. 1995). Following this procedure, we found that only three oscillating modes (CI, CIII, and CIV) are needed to represent the dominant fluctuations at all these locations. Figure 4 shows the time series at these locations from the detrended HC anomalies and those reconstructed from the three POP modes. It is apparent that the two sets of curves are highly consistent for all these locations and most of the variations, even the very high-frequency signals, are accounted for.

Apart from accounting for most of the variability in these chosen regions, each of these three modes seems to represent an independent pattern because their time coefficients are not significantly correlated with each other. Considering these properties as well as that the remaining modes make little contribution to the variability in the concerned region, we will concentrate on these three modes only for the following discussion. This is also justified because the remaining modes are not stable as the degrees of freedom in the subspace are changed.

After having identified the POP modes, it is generally useful to search for related signals in other relevant

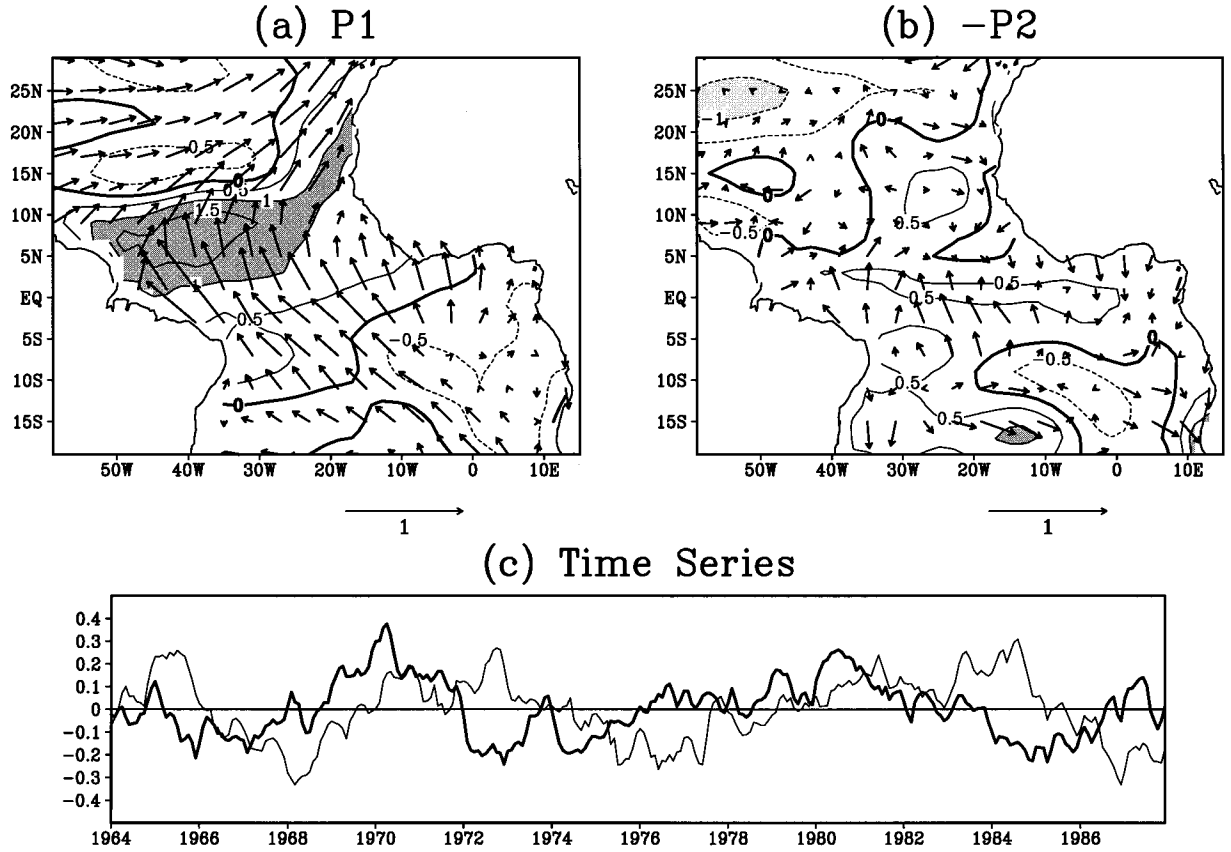

FIG. 5. The POP mode for the decadal variability of the simulated HC anomalies (CI). The real component (P1) is in (a); the negative imaginary component (−P2) in (b). Their corresponding time series are presented in (c) with the thick curve for P1 and thin curve for P2. The vectors plotted on (a) and (b) are associated patterns of wind stress anomalies. The contour interval in (a) and (b) is 0.5°C with regions greater than 1°C darkly shaded and less than −1°C lightly shaded. The vector at the bottom of (a) or (b) represents 1 dyn cm^{-2}. Note that the magnitude of the mode at any time equals the spatial mode in (a) or (b) multiplied by its corresponding time coefficient in (c).

variables. The patterns of these variables corresponding to the POP modes (referred to as the associated pattern) can be derived through a multivariate regression fit of the variable under consideration to the time series of all the POP modes (von Storch et al. 1988). This multivariate treatment is necessary because the POP time series are correlated with each other. Following this procedure, we have derived the associated patterns of all the POP modes for the anomalies of the zonal and meridional wind stress, SST, and surface heat flux. In an attempt to explain the underlying physical processes, these associated patterns will be presented with the corresponding POP modes.

c. Decadal variability

Based on the above analysis, the decadal signals of the anomalous HC variability can be represented by one POP mode (CI). Figure 5 shows the two components of this mode and their time series. The associated patterns of the zonal and meridional surface wind stresses are superimposed as a vector. For the convenience of explanation, the negative of the imaginary component ($-p2$, corresponding to A6 and A7 in the appendix) is plotted in Fig. 5b so that Fig. 5a and 5b can be viewed as an evolving sequence. This mode alone explains the largest amount (28%) of the anomalous HC variance (Table 1).

The spatial patterns of this mode are dominated by large-scale HC anomalies associated with the basinwide fluctuations of tropical trade wind systems. In one phase of the long-term oscillation (Fig. 5a), high anomalous HC (warm water) is built up in a belt around 0°–10°N in the central and western ocean, which extends northeastward to the North African coast. At the same time, negative HC anomalies are found in the Gulf of Guinea and along the Angolan coast. There is another region of negative anomalies in the northwestern ocean to the north of 10°N.

This distribution of HC anomalies is associated with a pattern of simultaneously weaker northeast and stronger southeast trade winds. In the western ocean to the north of the equator, the HC anomalies appear to be related to the Ekman pumping induced by simultaneous changes of the northeast and southeast trades, as well as its subsequent effects on the thermocline depth.

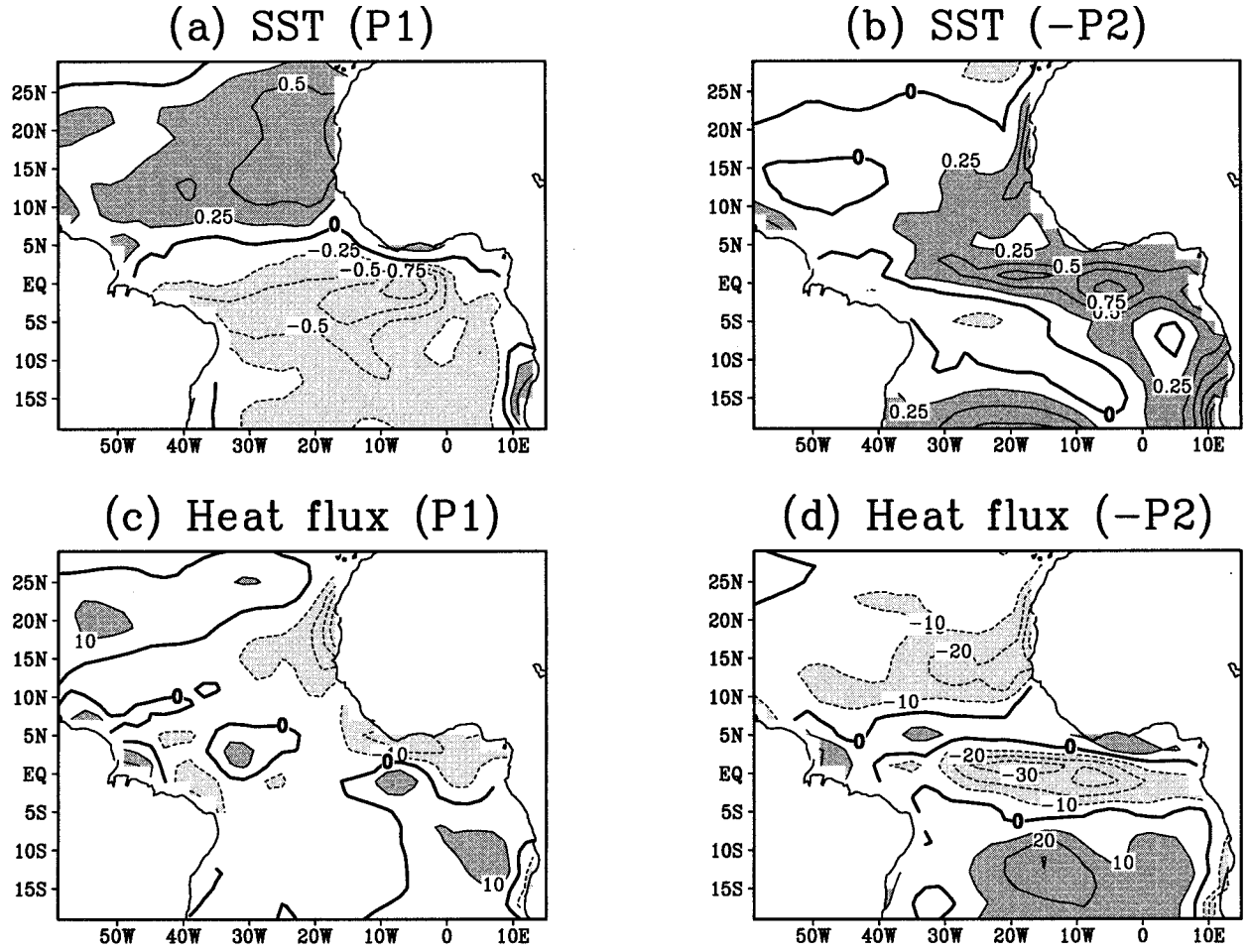

FIG. 6. The patterns of SST and surface heat flux anomalies associated with the decadal POP mode of HC anomalies (CI). The patterns associated with the real component (P1) are in (a) for SST and in (c) for the heat flux. The ones associated with the imaginary component (−P2) are in (b) for SST and (d) for the heat flux. The contour interval is 0.25°C for (a) and (b) with regions larger than 0.25°C darkly shaded and less than −0.25°C lightly shaded. For (c) and (d) the interval is 10 W m^{-2} with regions larger than 10 W m^{-2} darkly shaded and less than −10 W m^{-2} lightly shaded. The magnitude of the patterns at any time is equal to the spatial mode presented here multiplied by its corresponding time coefficient in (c) of Fig. 5.

Around the North African coast, the anomalies are related to reduced coastal upwelling due to a weaker alongshore wind component as part of the basinwide weakening of the northeast trade winds. In the Gulf of Guinea and along the southeastern coast, however, the changes are not strongly related to the local wind stress. They must be produced as a part of the basinwide adjustment of the upper-ocean thermal structure, in response to the changes in the trade winds.

In the next phase (Fig. 5b), HC anomalies become weaker and less organized. This pattern is also accompanied by weak wind anomalies without much coherent spatial structure. It seems that, as the anomalous pattern of the northeast/southeast trade winds weakens, the warm water accumulated in the northern ocean is exported through the equatorial wave guide into the southern ocean. This speculation is supported by a belt of relatively high HC anomalies along the equator, which seems to mark the pathway of this anomalous heat transport. At this stage, there is no apparent relationship between the surface wind forcing and the oceanic heat content anomalies. The atmosphere and the ocean seem to be decoupled and the state of the ocean is mainly decided by its previous state instead of by the contemporaneous forcing.

An examination of the two time series of the real and imaginary components (Fig. 5c) shows that they are dominated by variations with timescales of about ten years with a phase lag of 90°. Actually, the amplitude of the real component (Fig. 5c, thick curve) shows fluctuations similar to those of the DP index (Fig. 2b). The associated SST pattern at this stage (Fig. 6a) also has a well defined dipole structure, with positive anomalies spreading from the North African coast into the northern ocean and negative anomalies in the south. In the following stage (Fig. 6b), however, the SST anomalies as-

sociated with the imaginary component of the POP mode is drastically different from the previous one. The dipole pattern is not recognizable any more. The SST is dominated by positive anomalies along the equator and the eastern coast.

The patterns of SST anomalies are quite different from those of the HC. The HC anomalies are associated with heat accumulation in the western ocean, but the SST anomalies are dominated by changes in the upwelling at the North African coast and around the equatorial ocean. It is likely that the fluctuations of the surface heat flux have some effect on the formation of the dipole pattern. For instance, SST anomalies to the north of 10°N seem to be associated with the change of net heat flux into the ocean (Fig. 6c), which is mainly due to changes in evaporative cooling modulated by fluctuations of the northeast trade winds (Xie and Philander 1994; Robertson et al. 1995).

One should note that although the real component of the decadal POP mode shows robust spatial and temporal structure, its imaginary component is more sensitive to the change of the EOF subspace. In particular, the belt of the positive HC anomaly along the equator as seen in Fig. 5b is not present in the patterns derived from the analyses with more degrees of freedom. One possible explanation of this sensitivity is that the discharge of HC anomaly as shown in Fig. 5a is in fact accomplished by a series of continuously stimulated equatorial wave processes and the pattern shown in Fig. 5b represents the integrated effect of all these processes. With the increase in the number of degrees of freedom, however, these equatorial processes may be represented as new higher-frequency modes.

We briefly summarize features of CII, which also has relatively long period. The spatial structures of CII have some similarity to those of CI. Its time series, however, do not show significant phase lag between the real and imaginary components except during brief periods in 1966–70 and 1978–80. Moreover, the time series of the imaginary component have a large interannual component that is quite different from the designated period of CII. Overall, it is hard to find a physical interpretation for this behavior. Due to these problems and its short decay time, the mode seems to be ill-defined.

On the other hand, both real modes (RI and RII) represent changes of the meridional troughs and ridges. Their time series show that these changes are on timescales longer than those of CI. In fact, the structure of these modes have some similarity to the spatial distribution of the rates of linear trend that are removed from the data and the detrending process may have strong effects on their behavior. As we have mentioned above, these two modes are significantly correlated with each other and may not be interpreted separately. Whether the long-term variability represented by these modes is realistic needs to be further analyzed with longer-term simulations.

d. Interannual variability

The interannual signals can be represented by two POP modes (CIII and CIV). As shown in Table 1, these modes have periods about 1½ yr and 3 yr and explain 14% and 19% of the total variance, respectively. Combined, they account for about 30% of the total variance, which is close to the sum of the variance percentages. Therefore, it seems that these two modes are independent of each other.

The temporal and spatial structure of the higher-frequency mode (CIV), as well as its associated wind pattern (Fig. 7), exemplify the response of the tropical Atlantic Ocean to the fluctuations in the equatorial winds. In particular, when an easterly wind anomaly appears in the western ocean with maximum at the equator, as shown by the vectors in Fig. 7a, it generates cold oceanic anomalies propagating eastward as equatorial Kelvin waves and, at the same time, produces off-equatorial warm anomalies through the anomalous wind stress curl (Chao and Philander 1993), which tend to propagate westward as Rossby waves. As a result, the thermocline shoals in the eastern equatorial ocean and deepens in the western ocean, an effect which is most pronounced at regions off the equator (Fig. 7a).

As the wind anomaly weakens and reverses direction (Fig. 7b), the warm water accumulated in the west is first transported to the east by oceanic Kelvin waves, then propagates along the African coast as coastal Kelvin waves. At the same time, the cold signals from the earlier stage are propagating westward to the south and north of the equator, as reflected Rossby wave signals from the eastern coast (Fig. 7b). The most significant feature of this mode is its highly symmetric structure about the equator. The time series of this mode is dominated by strong year-to-year fluctuations (Fig. 7c), characteristic of the equatorial variability in the Atlantic Ocean.

The associated patterns of the SST and heat flux anomalies corresponding to each stage of CIV are shown in Fig. 8. In the period when the thermocline is shallow in the east, the SST anomalies are negative in the equatorial ocean and around the eastern coast (Fig. 8a). Following the discharge of the warm water to the east, the equatorial SST anomalies become positive (Fig. 8b). The anomalies of the surface heat flux, however, generally have a sign opposite to the SST anomalies (Figs. 8c, d), suggesting that the surface heat flux acts mainly to damp the dynamically generated SST anomaly. In reality, variations represented by this mode are very likely to be caused by air–sea interactions. And the wind changes could be a response to the equatorial HC and SST fluctuations (Zebiak 1993).

The structure of the lower-frequency mode (CIII), however, is more complicated (Fig. 9). In a sense, it is similar to the CIV discussed above because it also features the tropical ocean's response to equatorial wind fluctuations. In the phase represented by the real com-

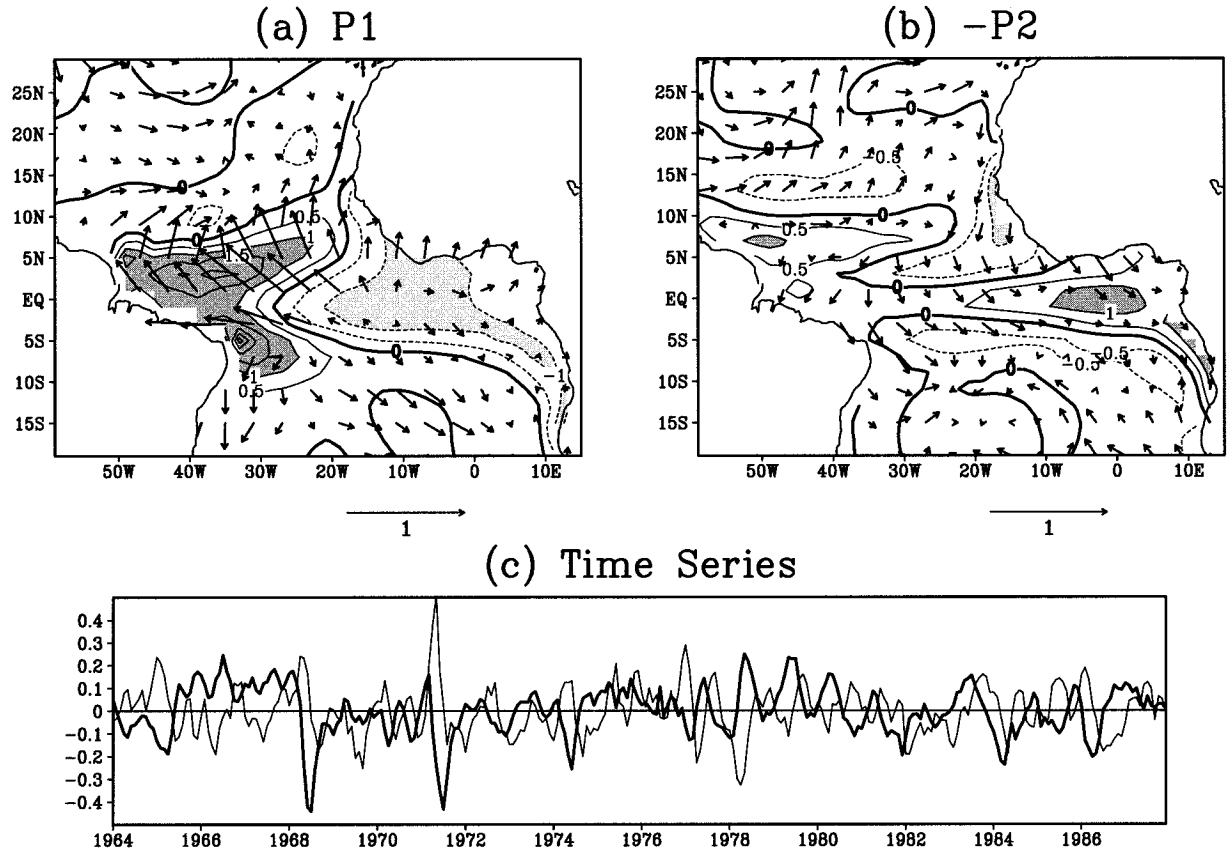

FIG. 7. As in Fig. 5 but for the higher-frequency interannual POP mode (CIV).

ponent (Fig. 9a), there is large contrast between the HC anomalies in the eastern and the western parts of the ocean, associated with easterly wind anomalies in the western equatorial ocean. In the following phase, the positive HC anomalies in the west propagate eastward through the equatorial waveguide, associated with the reversal of the equator wind anomalies (Fig. 9b). The associated SST anomalies are mainly near the equator and the eastern coast and generally in phase with the HC fluctuations. The fluctuation of the heat flux, however, is out-of-phase with that of the SST anomalies (not shown here).

What distinguishes this mode from the higher-frequency mode is its broader meridional structures in both the HC and wind anomalies. The broader meridional structure of CIII may be responsible for its longer periods of variability (Fig. 9c) because Rossby waves with slower propagation speed are generated (McCreary 1983). Another feature distinguishing CIII and CIV is that the former shows less symmetry between the anomalies in the north and the south. As seen from Fig. 9a, the HC and wind anomalies seem to be more significant in the northern part of the ocean. This asymmetry has been noticed by Zebiak (1993) in a coupled ocean–atmosphere model and considered as one of the major differences between the Pacific ENSO cycle and the equatorial variability in the Atlantic Ocean.

It should be noted that the interannual variations discussed above are similar to the equatorial wave activities noticed in many previous observational and modeling studies. For instance, Moore et al. (1978) synthesized the development of the oceanic waves generated by the equatorial wind fluctuations over the Atlantic Ocean and discussed their effects on the seasonal change in the ocean. Servain et al. (1982) further investigated the relationship between interannual zonal wind fluctuations in the central and western ocean and SST anomalies in the Gulf of Guinea. On the other hand, Carton and Huang (1994) described the equatorial heat content propagation during the tropical Atlantic warm events in 1984 and 1987–88. The feedbacks between the ocean and the atmosphere have also been examined by Zebiak (1993), who suggested that equatorial variability can be generated by unstable air–sea interaction in the tropical Atlantic region through a process similar to the ENSO cycle. Our results are generally in agreement with these previous studies.

On the other hand, we should point out that the propagation of equatorial HC anomalies is not equivalent to free oceanic waves. Although all HC variability can be

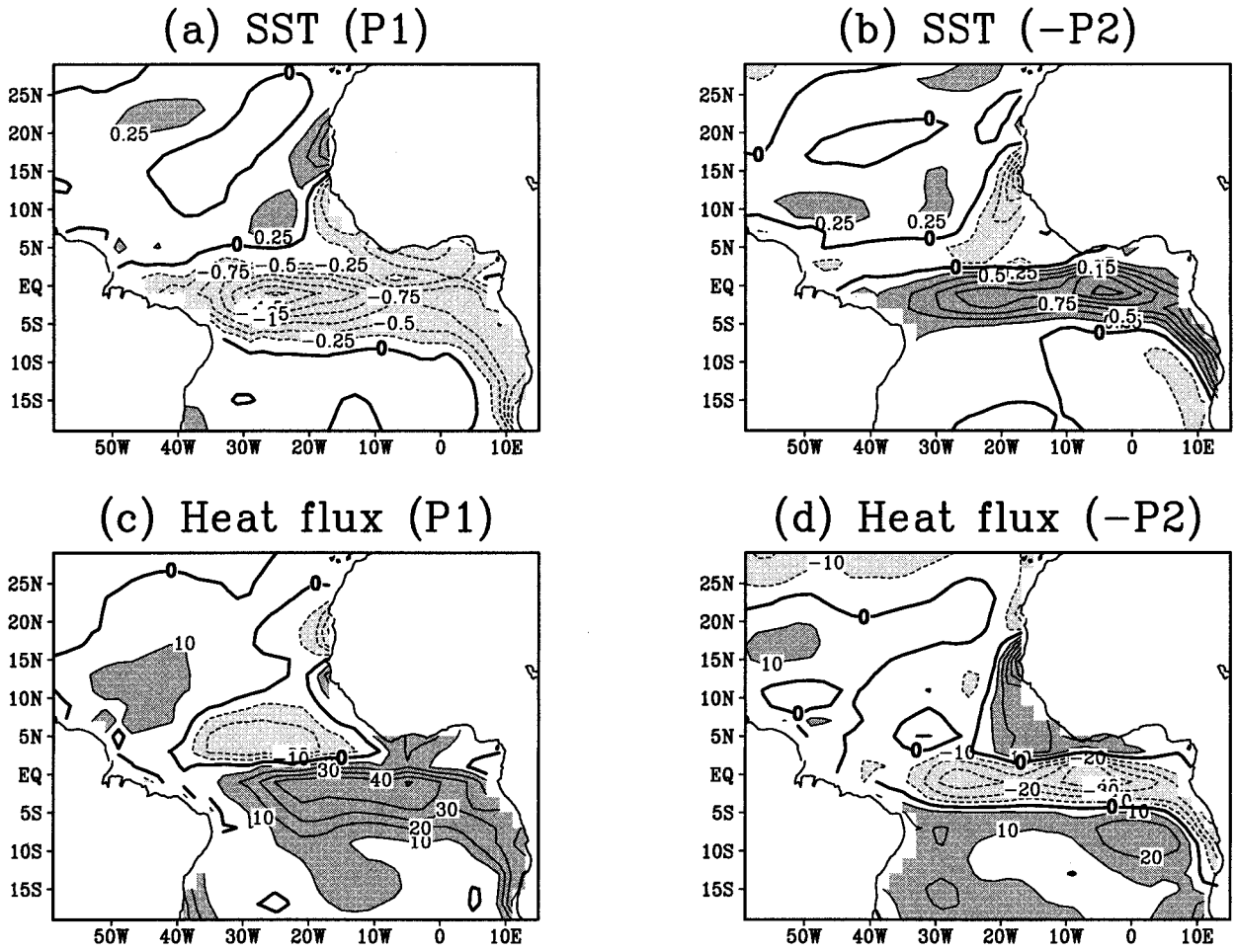

FIG. 8. As in Fig. 6 but for the higher-frequency interannual POP mode (CIV).

projected on equatorial wave modes, the wave concept may not be very effective in the Atlantic where a free wave cannot travel long before meeting a boundary. Therefore, an HC disturbance can arise by interference among a group of directly forced and reflected Kelvin and Rossby waves (Weisberg and Tang 1987; Chao and Philander 1993).

Previous studies have also noticed the seasonal dependence of the interannual signals in the equatorial ocean, which is not that easily discernable from these modes. We have conducted a variance analysis to the HC anomalies. It shows significant seasonality around the equator, associated with the ITCZ migration. The variance of the HC anomalies around the equator are largest in boreal summer seasons when the ITCZ is farthest north and the zonal wind should be annually strongest along the equator and smallest in boreal winter spring when the ITCZ is closest to the equator. North of the equator, the variance is increased in early boreal summer in midbasin and then propagates westward.

Overall, our analyses in this subsection suggest that there are two kinds of processes in generating SST and HC anomalies in the tropical Atlantic Ocean. The basic characteristics distinguishing these two processes are their different timescales and spatial structures. The interannual modes are characterized by periods of 2–3 yr, and are essentially confined to the equatorial waveguide and symmetric to the equator. They are forced by wind anomalies around the western equatorial ocean. The decadal mode with a period of about 10 yr, however, is asymmetric about the equator in its evolution, which is associated with the basinwide redistribution of the upper-ocean heat content in response to an out-of-phase fluctuation between the northeast and southeast trade winds. Associated with this variability, there should be significant heat transports between the southern and northern oceans.

We have conducted additional analyses to verify the above results. First, instead of using HC anomalies alone, we have conducted a combined EOF analysis of wind stress, heat content, SST, and net heat flux anomalies to provide the subspace for POP analysis. The results are quite comparable to those derived from the single variable analysis. In particular, the three POP

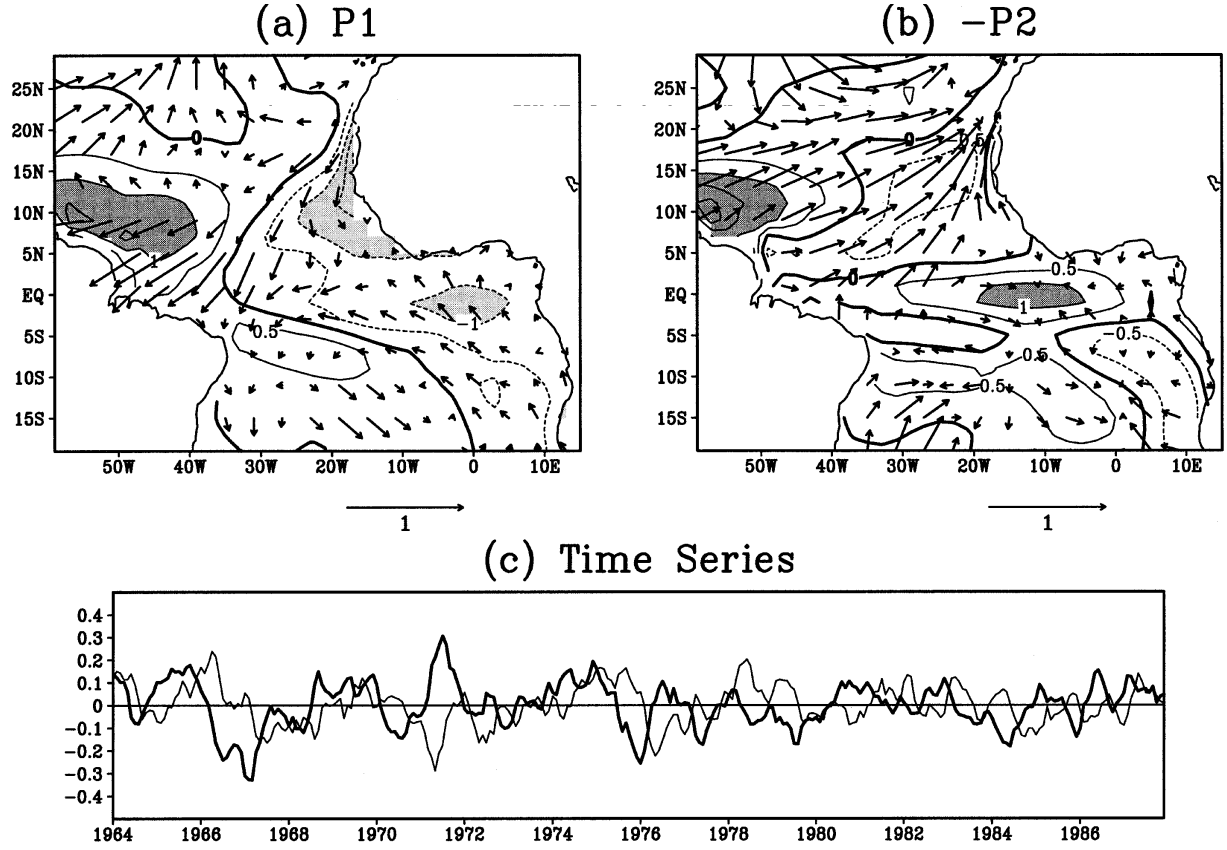

FIG. 9. As in Fig. 5 but for the lower-frequency interannual POP mode (CIII).

modes discussed above all have their counterparts in this combined analysis. We prefer using the HC fields because it is much smoother than the others. The combined modes have noisier temporal–spatial structure and shorter decay time, possibly due to including in constructing the transition matrix the wind stress data that are much less persistent than the HC fields.

We have also calculated POP modes on a seasonal basis. In this analysis, monthly HC anomalies are first averaged within a season. They are then grouped into four time sequences according to their seasons. In each sequence, there are 24 samples except for boreal winter, which has 23 samples. The POP analysis is applied to each sequence separately following the same procedure as we described before. The seasonal averaging and grouping procedure basically filters out signals with periods less than 2 yr so that modes with higher frequency like CIII and CIV are not well represented here. However, the lower-frequency signals, such as those represented by CI, should not be significantly affected by the filtering.

Our result shows that a POP mode with spatial and temporal structure like CI appears in every seasonal sequence except for boreal spring. Because of noise reduction by filtering, the decay times of these modes are generally longer than that of CI. For instance, the POP modes have periods around 9 yr and decay time about 4 yr in boreal winter and autumn. In boreal summer, the POP mode has period of 8.4 and a decay time of 8.3 yr. The longer decay time strengthens the oscillatory character of this mode. In boreal spring, however, the low-frequency signals are picked up by two modes with period of 7.5 and 12 yr respectively. Both, however, are not compatible with CI. The former mode is dismissed because it has small decay time (1.7 yr). The latter mode shows mostly symmetric structure in the real part although its imaginary part is somewhat similar to the CI. Overall, these calculations do suggest that the low-frequency variability as represented by CI is robust throughout most of the year though it seems to be most significant in boreal summer when the southeast trades are strongest.

5. The 1968 and 1984 warm events

After discussing the general modes of variability, we turn to examine the variations in the tropical Atlantic Ocean during specific periods, which are composed of the superposition of these different modes. As we have mentioned before, the tropical Atlantic experiences equatorial SST fluctuations in the eastern ocean with periods of 2–3 yr (see, e.g., Zebiak 1993). In a warm

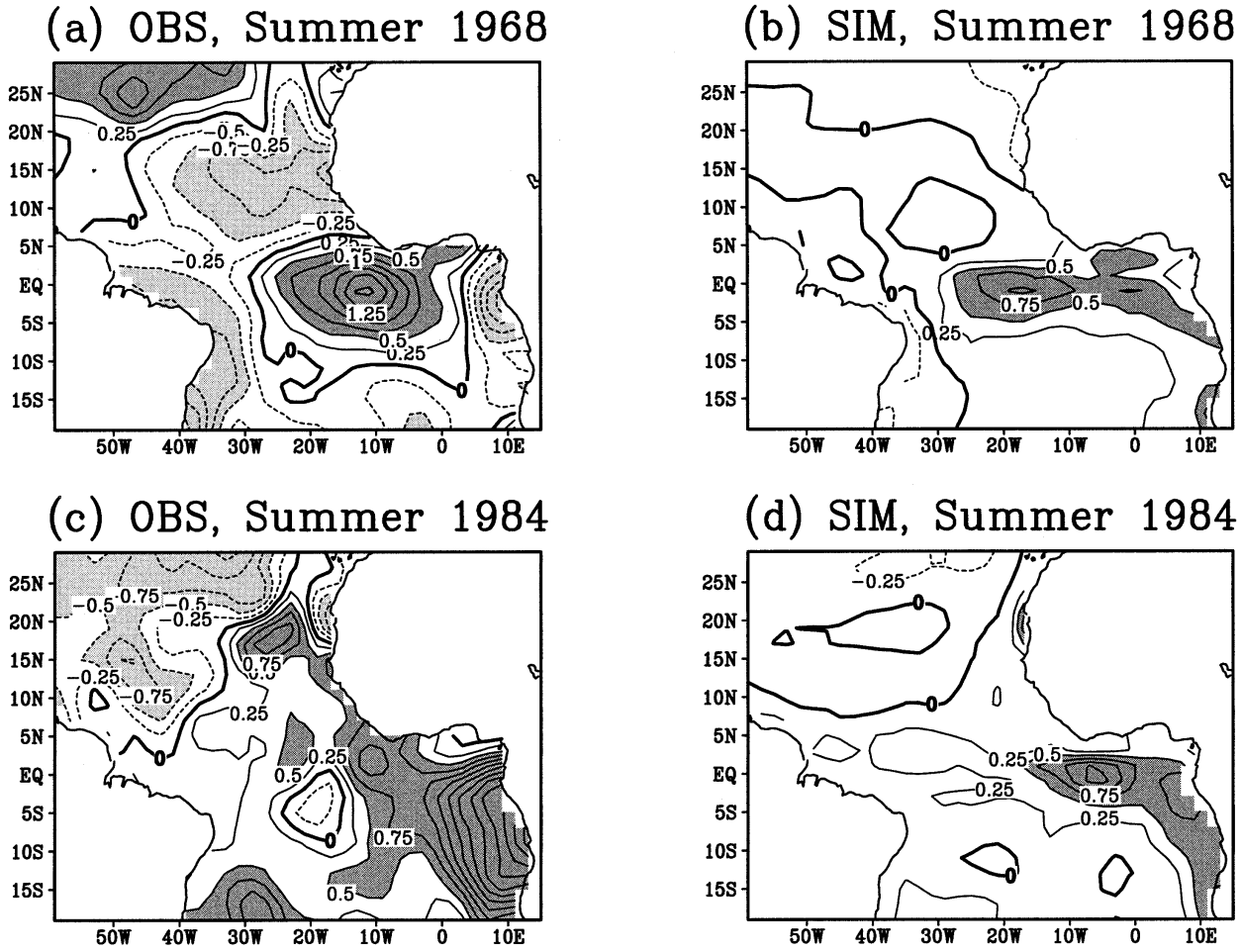

FIG. 10. Seasonally averaged SST anomalies for the boreal summer (Jun–Jul–Aug) of 1968 from (a) observations and (b) the simulation. The same quantities are shown in (c) and (d) for the summer of 1984. The contour interval is 0.25°C with regions larger than 0.25°C darkly shaded and less than −0.25°C lightly shaded.

event, positive SST anomalies appear in the Gulf of Guinea with a magnitude of 0.5°–1°C during boreal summer when the sea surface there should be coldest in a normal year (Carton and Huang 1994). These SST anomalies have been linked to the westerly wind anomalies in the western equatorial ocean (Servain et al. 1982; Hirst and Hastenrath 1983). In general, these anomalous events are a manifestation of the equatorial wave activity.

The warm event in 1984, however, was significantly different from this general picture. The magnitude of the observed SST anomalies is as high as 3°C in the boreal summer of 1984 (Fig. 10c), which is the largest for the period of our study and nearly twice the magnitude of the anomalies in the summer of 1968, the second strongest warm event in this period (Fig. 10a). Moreover, there are also significant differences in the spatial structure of these two warm events. The 1968 case is like the general picture described above with SST anomalies in the eastern and central ocean centered around the equator (Fig. 10a). The 1984 event, at its peak, had the largest SST anomalies in the southeast coastal region (Fig. 10c). Moreover, based on measurements during the SEQUAL/FOCAL experiments, the thermocline depth, which was anomalously deep in the boreal winter and spring in the eastern equatorial ocean, had returned to its normal position in the summer of 1984 (Katz et al. 1986). This difference in spatial structure between the two events is marginally reproduced in the simulation (Fig. 10b,d). However, as shown in the subsequent Figs. 11d and 12d, the structure of the simulated heat content anomalies is remarkably similar to the observed SST anomalies. We suspect that errors in SST anomalies may be due to inadequate heat flux parameterization as we discussed in section 2.

Since its occurrence, there have been many studies of the 1984 warm event, partly due to its extraordinary strength and partly because of more comprehensive measurements collected during the SEQUAL/FOCAL experiments. Most studies emphasize the similarity between the developments of this warm event and the El Niño in the Pacific Ocean (Philander 1986; Horel et al.

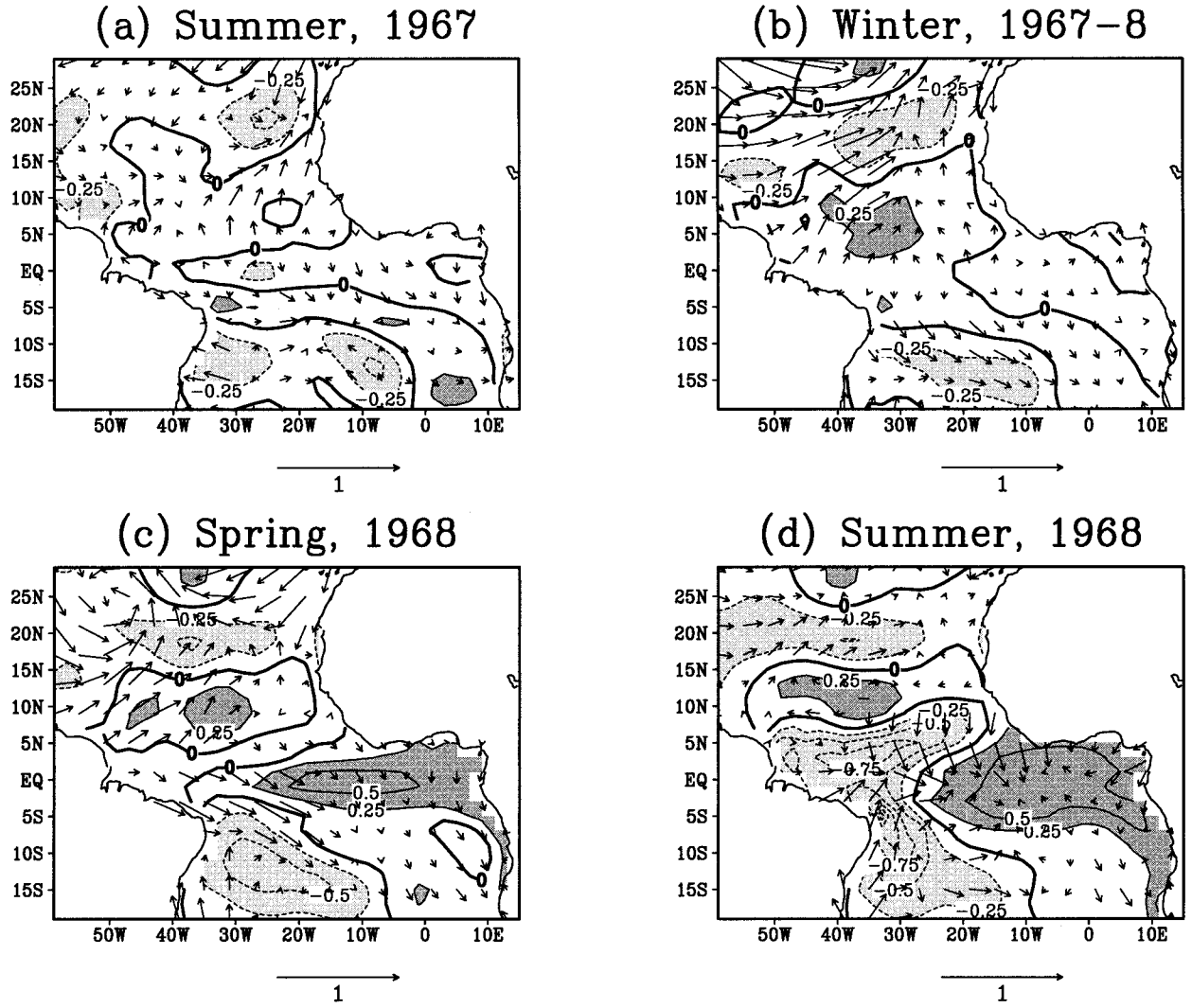

FIG. 11. Seasonally averaged simulated anomalous heat content and observed wind stress for 1967–68: (a) boreal summer 1967, (b) winter 1967/68, (c) spring 1968, and (d) summer 1968. The stress is given in dynes per square centimeter, while the contour interval is 0.25°C with regions larger than 0.25°C darkly shaded and less than −0.25°C lightly shaded.

1986, Carton and Huang 1994, Delecluse et al. 1994). However, the unique features of this event as we described above have not yet been explained. We suggest that variability in the tropical Atlantic Ocean is a result of the interference of variations with different periods. Here we give a comparison between the evolution of the 1968 and 1984 events to illustrate their differences.

Examining the historical development in the tropical Atlantic, we find little evidence of anomalous activities in the summer of 1967, which would lead to the warm event in 1968 (Fig. 11a). In fact, significant anomalous development started in the boreal winter of 1967/68, with warm HC anomalies appearing in the northern equatorial ocean, forced by a broad weakening of the northeast trades (Fig. 11b). The warming further developed in the following spring when the equatorial easterlies weakened and forced the warm water to the equatorial ocean through the waveguide (Fig. 11c). In the summer of 1968, positive anomalies in the eastern equatorial ocean reached their maximum value, so did the westerly wind anomalies in the western ocean. Associated with this wind pattern, negative HC anomalies formed both to the north and the south of the equator (Fig. 11d).

Decomposing this variation into the components of the three POP modes (not shown), we find that, during the warm event, the higher-frequency interannual mode (CIV) is most strongly manifested, which alone can account for a large part of the total variation. The lower-frequency interannual mode (CIII) also has some secondary effects, especially in the early period of the warming episode. The decadal mode (CI), however, makes little contribution.

On the other hand, the situation was quite different

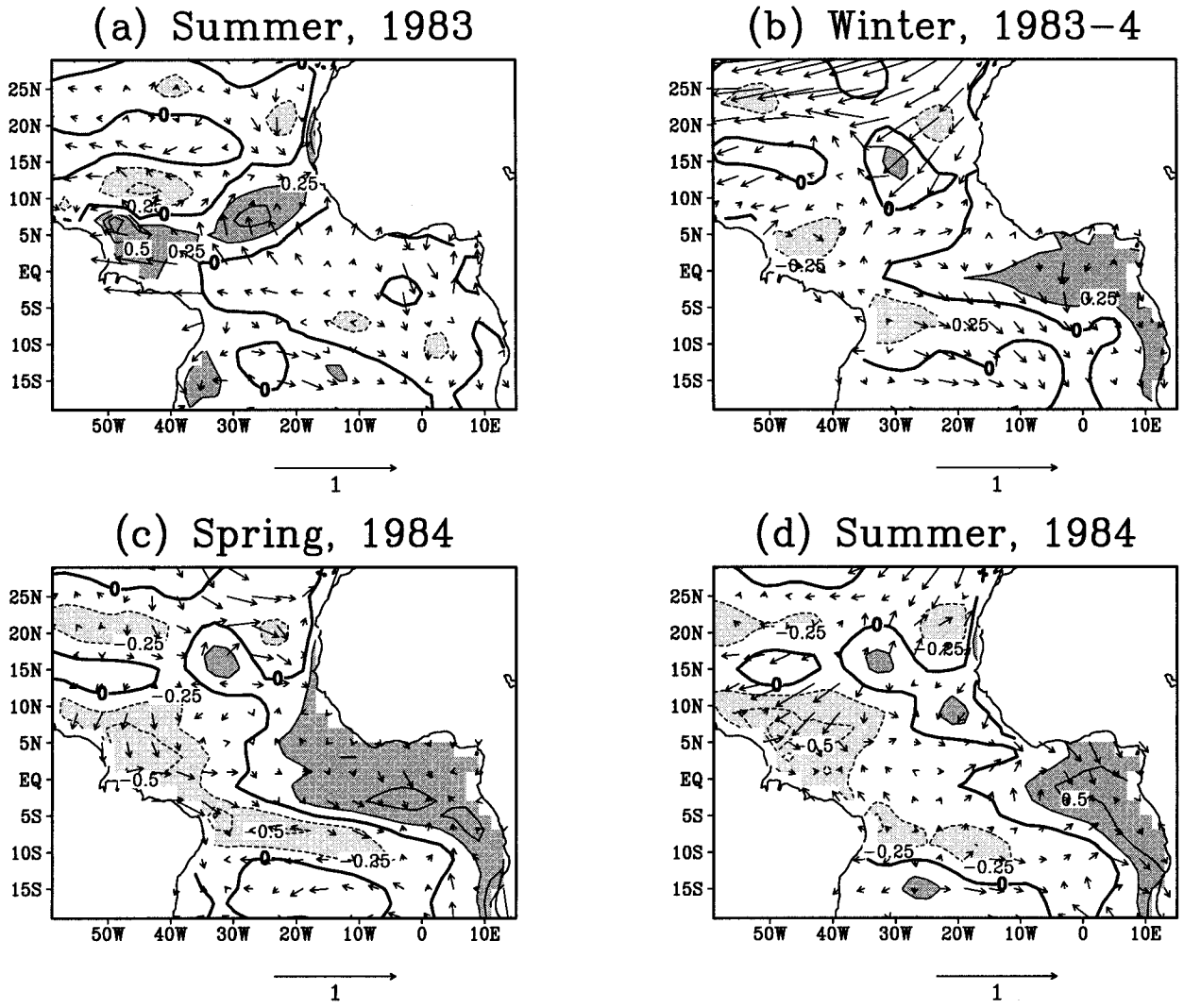

FIG. 12. Seasonally averaged simulated anomalous heat content and observed wind stress for 1983–84: (a) boreal summer 1983, (b) winter 1983/84, (c) spring 1984, and (d) summer 1984. The stress is given in dynes per square centimeter, while the contour interval is 0.25°C with regions larger than 0.25°C darkly shaded and less than −0.25°C lightly shaded.

for the 1984 warm event. There were significant signals as early as the boreal summer of 1983 when positive HC anomalies were already present in the northern ocean, forced by exceptionally strong easterlies around the equator (Fig. 12a). In the boreal winter of 1983/84, warm water propagated to the eastern ocean, associated with the weakening of the equatorial easterlies (Fig. 12b). The warm water then spread poleward along the coast during most of the spring season when the equatorial easterlies further weakened (Fig. 12c). By the summer of 1984, however, most of the heat anomalies ended up near the southeast coast (Fig. 12d). This process is very similar to the one described in Carton and Huang (1994).

Apart from its much earlier initiation and longer duration, the most striking feature in the evolution of the 1984 warm event is the strong asymmetry between the southern and the northern oceans in the summer of 1984. In fact, a decomposition of the HC field into its POP modes produces quite a different result from that of the 1968 event. In this case, every mode seems to have some role to play. In particular, the effects of the decadal mode are as important as each of the other two modes in causing the exceptionally warm anomalies near the southeast coast (Fig. 10c). It seems that the decadal pattern represented by Fig. 5a had reached its peak in the early 1980s (thick line, Fig. 5c) and was gradually evolving to its opposite phase (Fig. 5b, and the thin line in Fig. 5c). It is through the 1984 warm event that the transition process was completed and the pattern shown in Fig. 5a reached its new peak though with opposite sign compared to the early 1980s. We notice that this is also the time when both the observed and simulated DP indices reached their maxima after a quick transition

(Fig. 2b). In this sense, the anomalous oceanic conditions in the tropical Atlantic Ocean in the boreal summer of 1984 can be seen as an extreme phase of the decadal dipole pattern, as pointed out by Lamb et al. (1986).

6. Summary and discussion

A numerical simulation has been conducted using a general circulation model of the tropical Atlantic Ocean forced with observed monthly surface wind stress for 1964–87 and parameterized surface heat flux. The simulated sea surface temperature (SST) and upper-ocean heat content (HC) were used to examine the low-frequency variability in the ocean. A comparison with the SST observations shows that the model realistically reproduces the major features of the decadal variability at the sea surface, such as the fluctuation of the dipole pattern or the anomalous SST meridional gradient. The simulation, like the observations, also generates interannual SST variations with a period of 2–3 yr.

The simulated HC anomalies were used to examine the variations of the thermocline depth and the effects of ocean dynamics. A principal oscillation pattern (POP) analysis was used to distinguish the spatial structures of decadal and interannual modes of variability. It was found that the interannual modes are associated with equatorial oceanic disturbances stimulated by the fluctuations of the equatorial easterlies, which propagate eastward along the equator and westward in the north and south. The periods of these modes are determined by the meridional width of the equatorial wind anomaly. The decadal mode, however, is associated with the ocean's adjustment in response to the basinwide out-of-phase fluctuation between the northeast and southeast trade winds. For instance, associated with a weakening of the northeast and a simultaneous strengthening of the southeast trade winds, the thermocline deepens in a belt extending from 5°N in the west to the North African coast. At the same time, the thermocline shoals from the southeast coast to the equatorial ocean. The associated SST pattern has a strong dipole structure with positive anomalies in the north and negative anomalies in the south. When the wind anomalies weaken, the warm water accumulated in the northern ocean is redistributed within the basin. At this stage, the SST dipole disappears. Based on this classification, the extraordinarily large warm anomalies in the southeast ocean in the boreal summer of 1984 are the result of the positive interference of the decadal and interannual modes.

In general, these results suggest that it is possible to generate coherent dipole-like SST anomalies as a result of oceanic response to basinwide wind fluctuations. However, the dipole pattern described here is different from the traditional view based on the conventional EOF analyses that characterize the SST dipole as a standing oscillation or a north–south seesaw. Instead, based on our analysis, the dipole exists only during a certain stage of a long-term evolution of the redistribution in the oceanic heat content (Figs. 5 and 6).

The dipole-like SST anomalies result from different physical processes in different regions. In a situation like we described above, when the northeast trades weaken but the southeast trades strengthen, the positive SST anomalies in the northeastern ocean originate from reduced upwelling at the North African coast. The SST there is sensitive to small changes in the local thermocline depth, whereas the large displacement of the thermocline further to the west seems to have much less effect. Farther to the west, the SST anomalies are strengthened by the reduced evaporative heat loss due to weaker trade wind speed (Fig. 5a). The evaporative mechanism for off-equatorial SST changes was discussed by Xie and Philander (1994) and Robertson et a1.(1995).

To test this result, we conducted a sensitivity experiment in which the model was forced with the same wind stress but a different surface heat flux parameterization. This alternative parameterization follows Haney's (1971) formulation, consisting of a mean monthly climatological net heat flux plus a relaxation to observed SST monthly climatology with a fixed rate. In this case, there is no dependence on the wind speed of the evaporative heat loss at the sea surface. The results show that the dipole pattern is much weaker and significant SST anomalies are more confined to the east. The wind-induced evaporative cooling effects seem to be most significant in the northwestern part of the ocean.

As shown in Fig. 5a, negative anomalies appear in the southern and equatorial ocean when positive anomalies are in the north. Although the HC and SST anomalies in the northern ocean are mainly generated by local wind fluctuations, it is more likely that changes in the southeast are forced remotely since local wind fluctuations are rather weak. We believe that these oceanic anomalies are associated with a basinwide redistribution of the oceanic heat content. In this sense, the decadal anomalies in the southeastern part of the ocean are strongly related to what happens in the northern ocean.

Acknowledgments. Financial support for this research was provided by the National Oceanic and Atmospheric Administration under Grants NA26-GP0149 and NA46-GP0217 and by the National Science Foundation under Grant ATM-93-21354. The authors are grateful to Professor S.G.H. Philander for useful discussion during the course of this study, Drs. J.L. Kinter III and Y. Xue for helpful comments on the manuscript, and the two anonymous reviewers for constructive recommendations. We thank Drs. J. Servain and C. Penland for providing SST/wind stress datasets and the FORTRAN code of the POP analysis, respectively. We would also like to thank Dr. R. Yang for discussions about the usage of the POP method.

APPENDIX

Principal Oscillation Pattern (POP) Analysis

For a time-dependent M dimensional state vector $\mathbf{X}(t)$, where M may represent the number of grid points in space, or more generally the number of degrees of freedom of the system, a discretized linear model can be written as

$$\mathbf{X}(t + 1) = \mathbf{A}\mathbf{X}(t) + n(t), \tag{A1}$$

where $\mathbf{A}$ is an $M \times M$ matrix and $n(t)$ is the residual time series. Here $\mathbf{A}$ is computed statistically, assuming that the data follow a Markov process, so that

$$\mathbf{A} = (\overline{\mathbf{X}(t + 1)\ \mathbf{X}^{\mathrm{T}}(t)})(\overline{\mathbf{X}(t)\ \mathbf{X}^{\mathrm{T}}(t)})^{-1}, \tag{A2}$$

where the superscript T represents a transpose of a vector and the overbars denote averages over time.

The POP modes of the system (A1) are derived as the eigenvectors of $\mathbf{A}$. For the jth eigenvalue λ_j of the system $\mathbf{A}$, we have

$$\mathbf{A}\mathbf{p}_j = \lambda_j \mathbf{p}_j, \tag{A3}$$

where $\mathbf{p}_j$ is the corresponding eigenvector or the POP mode. Since $\mathbf{A}$ is not necessarily symmetric, the eigenvalues and eigenvectors can be either real or complex. However, because $\mathbf{A}$ is real, the complex eigenvalues and vectors come in conjugate pairs. In general, the state vector $\mathbf{X}(t)$ can be expressed in terms of these eigenvectors as

$$\mathbf{X}(t) = \sum_j \mathbf{z}_j(t)\mathbf{p}_j, \tag{A4}$$

where $\mathbf{z}_j(t)$ represents the time series of $\mathbf{p}_j$ that is determined following the procedure of Penland and Ghil (1993).

The contribution of a real eigenvector to $\mathbf{X}(t)$ is represented by the temporal fluctuation of a spatial pattern defined on the grid M. The contribution $\mathbf{P}(t)$ of a complex conjugate pair $\mathbf{p}$ and $\mathbf{p}^*$ (with the subscript j dropped) is more complicated. Notice that to keep $\mathbf{X}(t)$ real for any $\mathbf{p}$, the coefficients of the pairs of conjugate complex eigenvectors have to be complex conjugates too. Considering these properties, the contribution of a pair of complex modes ($\mathbf{p}$ and $\mathbf{p}^*$) can be written as

$$\mathbf{P}(t) = \mathbf{z}(t)\mathbf{p} + (\mathbf{z}(t)\mathbf{p})^*. \tag{A5}$$

Letting $\mathbf{p} = \mathbf{p}_1 + i\mathbf{p}_2$, and $\mathbf{z}(t) = \mathbf{z}_1(t) + i\mathbf{z}_2(t)$, we can expand (A5) to

$$\mathbf{P}(t) = 2(\mathbf{z}_1(t)\mathbf{p}_1 - \mathbf{z}_2(t)\mathbf{p}_2). \tag{A6}$$

In this paper, we refer to (A5) or (A6) as a complex POP mode.

The physical meaning of (A6) is discussed in detail by von Storch et al. (1988, 1995) and Blumenthal (1991). In general, if we write the corresponding complex eigenvalue as $\lambda = \rho\exp(-i\omega)$, the mode forms a damped oscillation between the two spatial patterns in the following consecutive order:

$$\cdots \rightarrow \mathbf{p}_1 \rightarrow -\mathbf{p}_2 \rightarrow -\mathbf{p}_1 \rightarrow \mathbf{p}_2 \rightarrow \mathbf{p}_1 \rightarrow \cdots, \tag{A7}$$

with the period $T = 2\pi/\omega$ for a complete cycle and the damping time $\tau = -1/\ln(\rho)$ during which the amplitude $|\mathbf{z}(t)|$ is reduced by a factor of $1/e$. On the other hand, a mode associated with a real eigenvalue (referred to as a real or damped mode) represents a spatial pattern that simply decays with the damping time.

REFERENCES

Blanke, B., and P. Delecluse, 1993: Variability of the tropical Atlantic Ocean simulated by a general circulation model with two different mixed layer physics. *J. Phys. Oceanogr.,* **23,** 1363–1388.

Blumenthal, B., 1991: Predictability of a coupled ocean–atmosphere model. *J. Climate,* **4,** 766–784.

Cardone, V. J., J. G. Greenwood, and M. A. Cane, 1990: On trends in historical marine wind data. *J. Climate,* **3,** 113–127.

Carton, J. A., and B. Huang, 1994: Warm events in the tropical Atlantic. *J. Phys. Oceanogr.,* **24,** 888–903.

Chao, Y., and S. G. H. Philander, 1993: On the structure of the Southern Oscillation. *J. Climate,* **6,** 450–469.

Delecluse, P., J. Servain, C. Levy, K. Arpe, and L. Bengtsson, 1994: On the connection between the 1984 Atlantic warm event and the 1982–1983 ENSO. *Tellus,* **46A,** 448–464.

Didden, N., and F. Schott, 1992: Seasonal variations in the western tropical Atlantic: Surface circulation from Geosat altimetry and WOCE model results. *J. Geophys. Res.,* **97,** 3529–3541.

Gu, D., and S. G. H. Philander, 1995: Secular changes of annual and interannual variability in the Tropics during the past century. *J. Climate,* **8,** 864–876.

Haney, R. L., 1971: Surface boundary condition for ocean general circulation models. *J. Phys. Oceanogr.,* **1,** 241–248.

Hasselmann, K., 1988: PIP and POPs: The reduction of complex dynamical systems using principal interaction and oscillation patterns. *J. Geophys. Res.,* **93,** 11 015–11 021.

Hastenrath, S., 1984: Interannual variability and annual cycle: Mechanisms of circulation and climate in the tropical Atlantic sector. *Mon. Wea. Rev.,* **112,** 1097–1107.

——, and L. Heller, 1977: Dynamics of climatic hazards in northeast Brazil. *Quart. J. Roy. Meteor. Soc.,* **103,** 77–92.

Hirst, A. C., and S. Hastenrath, 1983: Atmosphere–ocean mechanisms of climate anomalies in the Angola–Tropical Atlantic sector. *J. Phys. Oceanogr.,* **13,** 1146–1157.

Horel, J. D., V. E. Kousky, and M. T. Kagaro, 1986: Atmospheric conditions in the tropical Atlantic during 1983 and 1984. *Nature,* **322,** 243–245.

Houghton, R. W., and Y. Tourre, 1992: Characteristics of low-frequency sea surface temperature fluctuations in the tropical Atlantic. *J. Climate,* **5,** 765–771.

Huang, B., 1992: Numerical simulation of the seasonal and interannual variability of the tropical Atlantic Ocean circulation during the 1980s. Ph. D dissertation, University of Maryland, College Park, 209 pp. [Available from Dept. of Meteorology, University of Maryland, College Park, MD 20742.]

——, and J. Shukla, 1996: A comparison of two surface wind stress analyses over the tropical Atlantic during 1980–87. *J. Climate,* **9,** 906–927.

——, J. A. Carton, and J. Shukla, 1995: A numerical simulation of the variability in the tropical Atlantic Ocean, 1980–88. *J. Phys. Oceanogr.,* **25,** 835–854.

Katz, E. J., 1987: Seasonal response of the sea surface to the wind in the equatorial Atlantic. *J. Geophys. Res.,* **92,** 1885–1893.

——, P. Hisard, J.-M. Verstraete, and S. L. Garzoli, 1986: Annual change of sea surface slope along the equator of the Atlantic Ocean in 1983 and 1984. *Nature,* **322,** 245–247.

Lamb, P. J., 1978a. Large-scale tropical Atlantic surface circulation patterns associated with subsaharan weather anomalies. *Tellus,* **30,** 240–251.

——, 1978b: Case studies of tropical Atlantic surface circulation pattern during recent sub-Sahara weather anomalies, 1967–1968. *Mon. Wea. Rev.,* **106,** 482–491.

——, and R. A. Peppler, 1991: West Africa. *Teleconnections Linking Worldwide Climate Anomalies,* M. Glantz, R. Katz, and N. Nicholls, Eds, Cambridge University Press, 121–189.

——, ——, and S. Hastenrath, 1986: Interannual variability in the tropical Atlantic. *Nature,* **322,** 238–240.

Levitus, S., 1982: *Climatological Atlas of the World Ocean*. NOAA Prof. Paper No. 13, U.S. Govt. Printing Office, Washington, DC, 173 pp. [Available from National Oceanographic Data Center, NOAA/NESDIS, 1825 Connecticut Ave. NW, Washington, DC 20235.]

Lough, J. M., 1986: Tropical Atlantic sea surface temperature and rainfall variations in subsaharan Africa. *Mon. Wea. Rev.,* **114,** 561–570.

McCreary, J. P., 1983: A model of tropical ocean–atmosphere interaction. *Mon. Wea. Rev.,* **111,** 370–387.

Mehta, V. M., and T. Delworth, 1995: Decadal variability of the tropical Atlantic Ocean surface temperature in shipboard measurements and in a global ocean–atmosphere model. *J. Climate,* **8,** 172–190.

Mitchell, T. P., and J. M. Wallace, 1992: On the annual cycle in equatorial convection and sea-surface temperature. *J. Climate,* **5,** 932–952.

Moore, D. W., P. Hisard, J. P. McCreary, J. Merle, J. J. O'Brien, J. Picaut, J.-M. Verstrate, and C. Wunsch, 1978: Equatorial adjustment in the eastern Atlantic. *Geophys. Res. Lett.,* **5,** 637–640.

Moura, A. D., and J. Shukla, 1981: On the dynamics of the droughts in northeast Brazil: Observations, theory and numerical experiments with a general circulation model. *J. Atmos. Sci.,* **38,** 2653–2675.

Nobre, P., and J. Shukla, 1996: Variations of sea surface temperature, wind stress, and rainfall over the tropical Atlantic and South America. *J. Climate,* **9,** 2464–2479.

Oberhuber, J. M., 1988: An atlas based on the 'COADS' data set: The budgets of heat, buoyancy and turbulent kinetic energy at the surface of the global ocean. Max-Planck-Inst für Meteorology Rep. 15, 199 pp. [Available from Max-Planck Institut für Meteorologie, Bundestrasse 55, D-20146 Hamburg, Germany.]

Oort, A. H., 1983: Global atmospheric circulation statistics, 1958–1973. NOAA Prof. Paper No. 14, U.S. Govt. Printing Office, Washington, DC, 180 pp.

Pacanowski, R. C., and S. G. H. Philander, 1981: Parameterization of vertical mixing in numerical models of tropical oceans. *J. Phys. Oceanogr.,* **11,** 1443–1451.

——, K. Dixon, and A. Rosati, 1993: The GFDL modular ocean model users guide, version 1.0. GFDL Ocean Group Tech. Rep., No. 2. [Available from GFDL/NOAA, Princeton University, Princeton, NJ 08542.]

Penland, C., and M. Ghil, 1993: Forecasting northern hemisphere 700-mb geopotential height anomalies using empirical normal modes. *Mon. Wea. Rev.,* **121,** 2355–2372.

Philander, S. G. H., 1986: Unusual conditions in the tropical Atlantic Ocean in 1984. *Nature,* **322,** 236–238.

——, 1990: *El Niño, La Niña, and the Southern Oscillation*. Academic, 293 pp.

——, and R. C. Pacanowski, 1986: A model of the seasonal cycle in the tropical Atlantic Ocean. *J. Geophys. Res.,* **91**(C12), 14 192–14 206.

Rebert, J. P., J. R. Donguy, G. Eldin, and E. Wyrtki, 1985: Relations between sea level, thermocline depth, heat content, and dynamic height in the tropical Pacific Ocean. *J. Geophys. Res.,* **90,** 11 719–11 725.

Reverdin, G., P. Delécluse, C. Lévy, P. Andrich, A. Morlière, and J. M. Verstraete, 1991: The near surface tropical Atlantic in 1982–1984: Results from a numerical simulation and a data analysis. *Progress in Oceanography,* Vol. 27, Pergamon, 273–340.

Richardson, P., and S. G. H. Philander, 1987: The seasonal variation of surface currents in the tropical Atlantic Ocean: A comparison of ship drift data with results from a general circulation model. *J. Geophys. Res.,* **92,** 715–724.

Robertson, A. W., C.-C. Ma, C. R. Mechoso, and M. Ghil, 1995: Simulation of the tropical Pacific climate with a coupled ocean–atmosphere general circulation model. Part II: Interannual variability. *J. Climate,* **8,** 1178–1198.

Rosati, A., and K. Miyakoda, 1988: A general circulation model for upper ocean simulation. *J. Phys. Oceanogr.,* **18,** 1601–1626.

Schott, F., and C. W. Böning, 1991: The WOCE model in the western equatorial Atlantic: Upper layer circulation. *J. Geophys. Res.,* **96,** 6993–7004.

Seager, R., S. E. Zebiak, and M. A. Cane, 1988: A model of the tropical Pacific sea surface temperature climatology. *J. Geophys. Res.,* **93,** 1265–l280.

Servain, J., 1991. Simple climatic indices for the tropical Atlantic Ocean and some applications. *J. Geophys. Res.,* **96**(C8), 15 137–15 146.

——, and D. M. Legler, 1986: Empirical orthogonal function analysis of tropical Atlantic sea surface temperature and wind stress: 1964–1979. *J. Geophys. Res.,* **91,** 14 181–14 191.

——, J. Picaut, and J. Merle, 1982: Evidence of remote forcing in the equatorial Atlantic Ocean. *J. Phys. Oceanogr.,* **12,** 457–463.

——, ——, and A. J. Busalacchi, 1985: Interannual and seasonal variability of tropical Atlantic Ocean depicted by sixteen years of surface temperature and wind stress. *Coupled Ocean–Atmosphere Models,* J. C. J. Nihoul, Ed. Elsevier, 211–237.

——, M. Seva, S. Lukas, and G. Rougier, 1987: Climatic atlas of the tropical Atlantic wind stress and sea surface temperature: 1980–1984. *Ocean Air Interact.,* **1,** 109–182.

Trenberth, K. E., W. G. Large, and J. G. Olson, 1990: The mean annual cycle in global ocean wind stress. *J. Phys. Oceanogr.,* **20,** 1742–1760.

von Storch, H., T. Bruns, I. Fischer-Bruns, and K. Hasselmann, 1988: Principal oscillation pattern analysis of the 30- to 60-day oscillation in a general circulation model equatorial troposphere. *J. Geophys. Res.,* **93,** 11 022–11 036.

——, G. Bürger, R. Schnur, and J. von Storch, 1995: Principal oscillation patterns: A review. *J. Climate,* **8,** 377–400.

Wagner, R. G., and A. da Silver, 1994: Surface conditions associated with anomalous rainfall in the Guinea coastal region. *Int. J. Climatol.,* **14,** 179–199.

Wang, B., 1995: Interdecadal changes in El Niño onset in the last four decades. *J. Climate,* **8,** 267–285.

Weingartner, T. J., and R. H. Weisberg, 1991: A description of the annual cycle in sea surface temperature and upper ocean heat in the equatorial Atlantic. *J. Phys. Oceanogr.,* **21,** 83–96.

Weisberg, R. H., and T. Y. Tang, 1987: Further studies on the response of the equatorial thermocline in the Atlantic Ocean to the seasonally varying trade winds. *J. Geophys. Res.,* **92,** 3709–3727.

Xie, S., 1994: On the genesis of the equatorial annual cycle. *J. Climate,* **7,** 2008–2013.

——, and S. G. H. Philander, 1994: A coupled ocean–atmosphere model of relevance to the ITCZ in the eastern Pacific. *Tellus,* **46A,** 340–350.

Zebiak, S. E., 1993: Air–sea interaction in the equatorial Atlantic region. *J. Climate,* **8,** 1567–1586.